

# Early 2017 observations of TRAPPIST-1 with *Spitzer*

L. Delrez,<sup>1\*</sup> M. Gillon,<sup>2</sup> A. H. M. J. Triaud,<sup>3</sup> B.-O. Demory,<sup>4</sup> J. de Wit,<sup>5</sup>  
 J. G. Ingalls,<sup>6</sup> E. Agol,<sup>7,8</sup> E. Bolmont,<sup>9,10</sup> A. Burdanov,<sup>2</sup> A. J. Burgasser,<sup>11</sup>  
 S. J. Carey,<sup>6</sup> E. Jehin,<sup>2</sup> J. Leconte,<sup>12</sup> S. Lederer,<sup>13</sup> D. Queloz,<sup>1</sup> F. Selsis,<sup>12</sup>  
 and V. Van Grootel<sup>2</sup>

<sup>1</sup> Cavendish Laboratory, JJ Thomson Avenue, Cambridge, CB3 0HE, UK

<sup>2</sup> Space Sciences, Technologies and Astrophysics Research (STAR) Institute, Université de Liège, Allée du 6 Août 19C, B-4000 Liège, Belgium

<sup>3</sup> School of Physics & Astronomy, University of Birmingham, Edgbaston, Birmingham B15 2TT, United Kingdom

<sup>4</sup> University of Bern, Center for Space and Habitability, Gesellschaftsstrasse 6, CH-3012, Bern, Switzerland

<sup>5</sup> Department of Earth, Atmospheric and Planetary Sciences, Massachusetts Institute of Technology, 77 Massachusetts Avenue, Cambridge, MA 02139, USA

<sup>6</sup> IPAC, California Institute of Technology, 1200 E California Boulevard, Mail Code 314-6, Pasadena, California 91125, USA

<sup>7</sup> Astronomy Department, University of Washington, Seattle, WA, 98195, USA; Guggenheim Fellow

<sup>8</sup> NASA Astrobiology Institute's Virtual Planetary Laboratory, Seattle, WA, 98195, USA

<sup>9</sup> IRFU, CEA, Université Paris-Saclay, F-91191 Gif-sur-Yvette, France

<sup>10</sup> Université Paris Diderot, AIM, Sorbonne Paris Cité, CEA, CNRS, F-91191 Gif-sur-Yvette, France

<sup>11</sup> Center for Astrophysics and Space Science, University of California San Diego, La Jolla, CA, 92093, USA

<sup>12</sup> Laboratoire d'astrophysique de Bordeaux, Univ. Bordeaux, CNRS, B18N, Allée Geoffroy Saint-Hilaire, F-33615 Pessac, France

<sup>13</sup> NASA Johnson Space Center, 2101 NASA Parkway, Houston, Texas, 77058, USA

Accepted 2017 December 31. Received 2017 December 21; in original form 2017 October 12

## ABSTRACT

The recently detected TRAPPIST-1 planetary system, with its seven planets transiting a nearby ultracool dwarf star, offers the first opportunity to perform comparative exoplanetology of temperate Earth-sized worlds. To further advance our understanding of these planets' compositions, energy budgets, and dynamics, we are carrying out an intensive photometric monitoring campaign of their transits with the *Spitzer Space Telescope*. In this context, we present 60 new transits of the TRAPPIST-1 planets observed with *Spitzer*/IRAC in February and March 2017. We combine these observations with previously published *Spitzer* transit photometry and perform a global analysis of the resulting extensive dataset. This analysis refines the transit parameters and provides revised values for the planets' physical parameters, notably their radii, using updated properties for the star. As part of our study, we also measure precise transit timings that will be used in a companion paper to refine the planets' masses and compositions using the transit timing variations method. TRAPPIST-1 shows a very low level of low-frequency variability in the IRAC 4.5- $\mu$ m band, with a photometric RMS of only 0.11% at a 123-s cadence. We do not detect any evidence of a (quasi-)periodic signal related to stellar rotation. We also analyze the transit light curves individually, to search for possible variations in the transit parameters of each planet due to stellar variability, and find that the *Spitzer* transits of the planets are mostly immune to the effects of stellar variations. These results are encouraging for forthcoming transmission spectroscopy observations of the TRAPPIST-1 planets with the *James Webb Space Telescope*.

**Key words:** planetary systems – stars: individual: TRAPPIST-1 – techniques: photometric

## 1 INTRODUCTION

Small stars are beneficial for the discovery and study of exoplanets by transit methods (e.g. [Nutzman & Charbonneau 2008](#); [He et al. 2017](#)). For a given planet’s size and irradiation, they offer deeper planetary transits, and shorter orbital periods. The seven Earth-sized worlds orbiting the nearby ultracool dwarf star TRAPPIST-1 ([Gillon et al. 2016, 2017](#), hereafter [G16](#) and [G17](#) respectively) have become prime targets for the study of small planets beyond the Solar system, including the study of their atmospheres, owing to their transiting configuration combined with the infrared brightness ( $K=10.3$ ) and Jupiter-like size ( $\sim 0.12 R_{\odot}$ ) of their host star ([de Wit et al. 2016](#); [Barstow & Irwin 2016](#); [Morley et al. 2017](#)).

The TRAPPIST-1 planets have further importance. There are approximately three times as many M-dwarfs as FGK-dwarfs in the Milky Way ([Kroupa 2001](#); [Chabrier 2003](#); [Henry et al. 2006](#)), and small planets appear to surround M-dwarfs three to five times more frequently than Sun-like stars (e.g. [Bonfils et al. 2013](#); [Dressing & Charbonneau 2013, 2015](#)). If this trend continues to the bottom of the main-sequence (see [He et al. 2017](#)), the TRAPPIST-1 planets could well represent the most common Earth-sized planets in our Galaxy, which in itself would warrant special attention. TRAPPIST-1 also presents an interesting numerical and dynamical challenge; for example, assessing its stability on Gyr timescales for orbital periods that have day to week timescales ([Tamayo et al. 2016, 2017](#)).

A comparative study of the TRAPPIST-1 planets is aided by the fact that they all transit the same star. Because the knowledge of most planetary parameters (e.g., mass and radius) is dependent on knowing these parameters for their parent stars, it is often difficult to make accurate comparisons across systems. Although the parameters of the TRAPPIST-1 planets remain dependent on the parameters of their host star, we can nevertheless compare the planets to one another. Furthermore, the planets have emerged from the same nebular environment, have experienced a similar history in terms of irradiation (notably in the XUV range; [Wheatley et al. 2017](#); [Bourrier et al. 2017](#); [O’Malley-James & Kaltenegger 2017](#)), and similar volatile delivery and atmospheric sculpting via cometary impacts ([Kral et al. submitted](#)). Thus, any differences among the planets must be the result of distinctions in their development. One example would be the possible detection of  $O_2$ , which on Earth has biological origins but on other worlds can be produced abiotically through the photodissociation of water vapour and escape of hydrogen (e.g. [Wordsworth & Pierrehumbert 2014](#); [Bolmont et al. 2017](#)). The presence of significant  $O_2$  on only one of the seven planets would indicate a process particular to that planet, such as microbial respiration, with potentially far-reaching implications in humanity’s search for life beyond the Earth.

To improve the characterization of the planets in the TRAPPIST-1 system, and prepare for exploration of their atmospheric properties with the upcoming *James Webb Space Telescope* (JWST) mission ([Barstow & Irwin 2016](#); [Morley et al. 2017](#)), we are conducting an intensive, high-precision, space-based photometric monitoring campaign of the system with *Spitzer* (Exploration Program ID 13067). The main goals of this program are to improve the plan-

ets’ transit parameters - notably to refine the determination of their radii - and to use the measured transit timing variations (TTVs) to constrain their masses and orbits ([Agol et al. 2005](#); [Holman & Murray 2005](#)). Our *Spitzer* program also aims to study the infrared variability of the host star and its possible impact on the future JWST observations, and to obtain first constraints on the presence of atmospheres around the planets by comparing their transit depths measured in the infrared by *Spitzer* to the ones measured at shorter wavelengths by other facilities (e.g. [de Wit et al. 2016](#)).

In this paper, we present observations gathered during the Feb-Mar 2017 window of visibility of the star by *Spitzer*. These new data more than double the number of transit events observed on TRAPPIST-1 with *Spitzer*. Section 2 describes the data and data reduction. In Section 3, we combine these observations with previous *Spitzer* transit photometry of TRAPPIST-1 presented in [G17](#), and perform a global analysis that enables us to significantly improve the planets’ transit parameters. We also use updated physical parameters for the star ([Van Grootel et al. 2017](#)), to revise the planets’ physical parameters, notably their radii. In addition, we assess the low-frequency infrared variability of the star and its impact on our measured quantities. As part of our analysis, we also extract precise transit timings. Our TTV analysis of the current timing dataset, including these new *Spitzer* timings, the resulting updated planetary masses, and our interpretations on the planets’ composition and formation, are presented in a separate companion paper ([Grimm et al. 2017](#)). In Section 4, we discuss our results, examining variability in the transit parameters over the breadth of the dataset, and setting limits on wavelength-dependent transit depths for TRAPPIST-1b as a probe of its atmospheric properties. We summarize our results in Section 5.

## 2 OBSERVATIONS AND DATA REDUCTION

As part of our Warm *Spitzer* Exploration Science program (ID 13067), *Spitzer* monitored 9, 16, 9, 6, 4, 3, and 1 new transit(s) of TRAPPIST-1b, -1c, -1d, -1e, -1f, -1g, and -1h, respectively, in the  $4.5\text{-}\mu\text{m}$  channel of its Infrared Array Camera (IRAC, [Fazio et al. 2004](#)). Twelve additional transits of TRAPPIST-1b were also observed with IRAC in the  $3.6\text{-}\mu\text{m}$  channel. All these observations were performed between 18 Feb and 27 Mar 2017. The corresponding data can be accessed using the *Spitzer* Heritage Archive<sup>1</sup> (SHA). The observations were obtained in subarray mode ( $32 \times 32$  pixels windowing of the detector) with an exposure time of 1.92 s. They were made without dithering (continuous staring) and in the pointing calibration and reference sensor (PCRS) peak-up mode ([Ingalls et al. 2012](#)), which maximizes the accuracy in the position of the target on the detector so as to minimize the so-called “pixel phase effect” of IRAC indium antimonide arrays (e.g. [Knutson et al. 2008](#)). All the data were calibrated with the *Spitzer* pipeline S19.2.0, and delivered as cubes of 64 subarray images of  $32 \times 32$  pixels (pixel scale = 1.2 arcsec).

<sup>1</sup> <http://sha.ipac.caltech.edu>

Our photometric extraction was identical to that described in G17. After converting fluxes from MJy/sr to photon counts, we used the IRAF/DAOPHOT<sup>2</sup> software (Stetson 1987) to measure aperture photometry for the star within a circular aperture of 2.3 pixels. The apertures for each image were centered on the stellar point-spread function (PSF) by fitting to a 2D-Gaussian profile, which also yielded measurements of the PSF width along the  $x$  and  $y$  image coordinates. Images with discrepant measurements for the PSF center, background flux, or source flux were discarded as described in Gillon et al. (2014). We then combined the measurements per cube of 64 images. The photometric errors were taken as the errors on the average flux measurements for each cube.

We complemented the resulting set of light curves with the *Spitzer* transit photometry previously published in G17, consisting of 16, 11, 5, 2, 3, 2, and 1 transit(s) of TRAPPIST-1b, -1c, -1d, -1e, -1f, -1g, and -1h, respectively, all observed with IRAC at 4.5  $\mu\text{m}$ . We refer the reader to G17 and references therein for more details about these data.

Our extensive *Spitzer* dataset thus includes a total of 37, 27, 14, 8, 7, 5, and 2 transits of planets b, c, d, e, f, g, and h, respectively. A few of these light curves showed flare signatures for which we discarded the corresponding measurements.

### 3 DATA ANALYSIS

Our data analysis was divided into three steps. We first performed individual analyses of the transit light curves (Section 3.1) to select the optimal photometric model for each light curve, measure the transit timings, and assess the variability of the transit parameters for each planet due to stellar variability. We then performed a global analysis of the whole dataset (Section 3.2) with the aim of improving our knowledge of the system parameters. Finally, we used our extensive *Spitzer* dataset to assess the low-frequency infrared variability of the star in the IRAC 4.5- $\mu\text{m}$  channel (Section 3.3).

Our individual and global data analyses were all carried out using the most recent version of the adaptive Markov Chain Monte-Carlo (MCMC) code presented in Gillon et al. (2012, see also Gillon et al. 2014). We refer the reader to these papers and references therein for a detailed description of the MCMC algorithm and only describe below the aspects that are specific to the analyses presented here.

#### 3.1 Individual analyses

We first converted each UT time of mid-exposure to the BJD<sub>TDB</sub> time-scale, as described by Eastman et al. (2010). We then performed an individual model selection for each light curve, using the transit model of Mandel & Agol (2002) multiplied by a photometric baseline model, different for each light curve, aiming to represent the other astrophysical and instrumental effects at the source of photometric

variations. A quadratic limb-darkening law was assumed for the star. For each light curve, we explored a large range of baseline models and selected the one that minimizes the Bayesian Information Criterion (BIC, Schwarz 1978). This led us to first include a linear or quadratic function of the  $x$ - and  $y$ -positions of the stellar PSF center (as measured in the images by fitting a two-dimensional Gaussian profile) in the baseline model of every light curve to account for the pixel phase effect (e.g. Knutson et al. 2008). For some light curves, the modeling of this effect was improved by complementing the  $x$ - and  $y$ -polynomial with a numerical position model computed with the bi-linearly-interpolated sub-pixel sensitivity (BLISS) mapping method (Stevenson et al. 2012). The sampling of the position space (number of grid points) was selected so that at least five measurements were located in each sub-pixel box. We refer the reader to Gillon et al. (2014) for more details about the implementation of this approach in the MCMC code. We found that including a linear or quadratic function of the measured FWHM of the stellar PSF in the  $x$ - and/or  $y$ -directions resulted in a significant decrease in the BIC for most light curves (similar to Lanotte et al. 2014 and Demory et al. 2016). A polynomial of the logarithm of time was also required for some light curves to represent a sharp decrease of the detector response at the beginning of the observations (the so-called “ramp effect”, Knutson et al. 2008). Finally, a polynomial of time was also included in the baseline model for a fraction of the light curves to represent low-frequency signals likely related to the rotational variability of the star (see G16, Luger et al. 2017a, and Section 3.3).

For each individual analysis, the jump parameters of the MCMC, i.e. the parameters randomly perturbed at each step of the Markov chains, were as follows:

- The stellar mass  $M_\star$ , radius  $R_\star$ , effective temperature  $T_{\text{eff}}$ , and metallicity [Fe/H]. We assumed the normal distributions  $\mathcal{N}(0.0802, 0.0073^2) M_\odot$ ,  $\mathcal{N}(0.117, 0.0036^2) R_\odot$ ,  $\mathcal{N}(2559, 50^2)$  K, and  $\mathcal{N}(0.04, 0.08^2)$  dex as respective prior probability distribution functions (PDFs) for these four parameters based on the values given in G17.

- For each transit (some light curves cover several transits), the transit depth  $dF = (R_p/R_\star)^2$  where  $R_p$  is the radius of the transiting planet, the transit impact parameter  $b = a \cos i/R_\star$  where  $a$  is the orbital semi-major axis and  $i$  is the orbital inclination, the transit width  $W$  (defined as the duration from first to last contact), and the time of mid-transit  $T_0$ .

- The linear combinations of the quadratic limb-darkening coefficients ( $u_1, u_2$ ) in the considered bandpass,  $c_1 = 2 \times u_1 + u_2$  and  $c_2 = u_1 - 2 \times u_2$ . For each bandpass, values and errors for  $u_1$  and  $u_2$  were interpolated for TRAPPIST-1 from the tables of Claret & Bloemen (2011) and the corresponding normal distributions were used as prior PDFs.

For these individual analyses, we kept the orbital period(s) of the relevant planet(s) fixed to the value(s) reported in G17 (for TRAPPIST-1b, c, d, e, f, g) and Luger et al. (2017a, for TRAPPIST-1h). As in G17, we assumed circular orbits for all the planets (eccentricity  $e = 0$ ).

For each light curve, a preliminary MCMC analysis composed of one chain of 10 000 steps was first performed to estimate the correction factors  $CF$  to be applied to the photometric error bars, to account for both the over- or under-

<sup>2</sup> IRAF is distributed by the National Optical Astronomy Observatory, which is operated by the Association of Universities for Research in Astronomy, Inc., under cooperative agreement with the National Science Foundation.

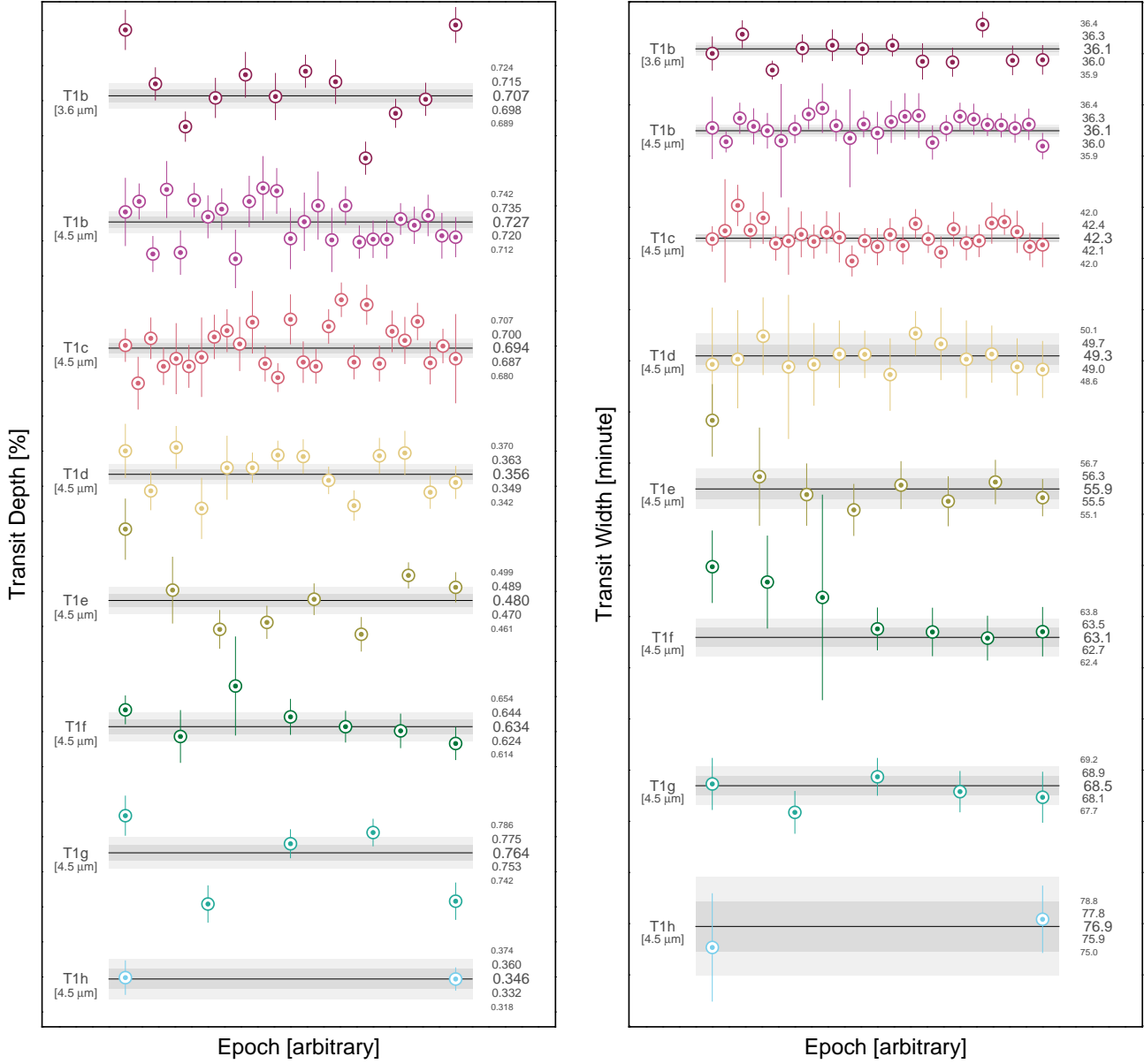


**Figure 1.** *Left:* Individual transit depth measurements for each of the events captured with *Spitzer*. The horizontal black line shows the median of the global MCMC posterior PDF (with its 1, and 2 $\sigma$  confidence, in shades of grey); the numerical values are also provided. Events are ranked in order of capture, left to right (but not linearly in time). *Right:* Similarly, but showing the duration of transit.

estimation of the white noise of each measurement and the presence of correlated (red) noise in the data (see Gillon et al. 2012 and Appendix B1 for details). Then, a longer MCMC analysis was performed, composed of two chains of 100 000 steps, whose convergence was checked using the statistical test of Gelman & Rubin (1992).

Table A1 presents for each planet the transit timings, depths, and durations deduced from the individual analyses of its transit light curves. For each planet, we performed a linear regression of the measured *Spitzer* transit timings as a function of their epochs to derive an updated mean transit ephemeris (given in Table 1). We show individual depths and durations in Fig. 1 and see that in general, they are compat-

ible to one another, epoch after epoch, following close to a normal distribution. Our individual uncertainties on the duration appear all slightly over-estimated when we compare them to the mean of individual measurements. All planets have reduced chi-squared  $\chi_r^2 < 1$  except for TRAPPIST-1b at 3.6  $\mu\text{m}$ , which has  $\chi_r^2 = 1.1$ . The situation is different for the transit depths. TRAPPIST-1b (4.5  $\mu\text{m}$ ), -1c, -1d, -1f, and -1h have  $\chi_r^2$  compatible with normal distribution, whereas TRAPPIST-1b (3.6  $\mu\text{m}$ ) has  $\chi_r^2 = 4.4$ , TRAPPIST-1e has  $\chi_r^2 = 2.4$ , and TRAPPIST-1g has  $\chi_r^2 = 4.3$ . We discuss these dispersions later in the text (Section 4.2).

### 3.2 Global analysis

In a second phase, we carried out a global MCMC analysis of all the TRAPPIST-1 transits observed by *Spitzer* to improve the determination of the system parameters. We first performed a preliminary analysis, composed of one chain of 10 000 steps, to determine the correction factors  $CF$  to be applied to the error bars of each light curve (see Gillon et al. 2012 and Appendix B1 for details). With the corrected error bars, we then performed the final global analysis, consisting of two Markov chains of 100 000 steps. The jump parameters in our global analysis were as follows:

- The stellar mass  $M_\star$ , radius  $R_\star$ , effective temperature  $T_{\text{eff}}$ , and metallicity  $[\text{Fe}/\text{H}]$ .
- The linear combinations  $c_1$  and  $c_2$  of the quadratic limb-darkening coefficients ( $u_1, u_2$ ) for each bandpass, defined as previously.
- For the seven planets, the transit depth  $dF_{4.5\mu\text{m}}$  at  $4.5 \mu\text{m}$ , and the transit impact parameter  $b$ . The transit duration was not a jump parameter anymore in the global analysis, as it is uniquely defined for each planet by its orbital period, transit depth, and impact parameter, combined with the stellar mass and radius (Seager & Mallén-Ornelas 2003). This assumption neglects orbital eccentricity and transit duration variations, which may be justified due to the small eccentricities expected when migrating into Laplace resonances (Luger et al. 2017a), and the small amplitude of transit duration variations that is expected based on dynamical models.
- For TRAPPIST-1b, the transit depth difference between the *Spitzer*/IRAC  $3.6\text{-}\mu\text{m}$  and  $4.5\text{-}\mu\text{m}$  channels:  $ddF = dF_{3.6\mu\text{m}} - dF_{4.5\mu\text{m}}$ .
- For the six inner planets, the transit timing variation (TTV) of each transit with respect to the mean transit ephemeris derived from the individual analyses (cf. Section 3.1).
- For TRAPPIST-1h, the orbital period  $P$  and the mid-transit time  $T_0$ .

This gives a total of 122 jump parameters for 19 258 data points. As previously, we assumed circular orbits for all the planets. For  $M_\star$ , we used a normal prior PDF based on the mass of  $0.089 \pm 0.007 M_\odot$  semi-empirically derived by Van Grootel et al. (2017) for TRAPPIST-1 by combining a prior from stellar evolution models to a set of dynamical masses recently reported by Dupuy & Liu (2017) for a sample of equivalently classified ultracool dwarfs in astrometric binaries. We prefer here to assume this semi-empirical prior for the stellar mass rather than a purely theoretical one, like the one used previously in G16 and G17, as current stellar evolutionary models are known to underestimate the radii of some low-mass stars (e.g. Torres 2013, MacDonald & Mullan 2014, and references therein; see Van Grootel et al. 2017 for more details). We assumed the same normal prior PDFs as previously for  $[\text{Fe}/\text{H}]$ , and ( $u_1, u_2$ ) for both bandpasses. Uniform non-informative prior distributions were assumed for the other jump parameters.

The convergence of the chains was again checked with the statistical test of Gelman & Rubin (1992). The Gelman-Rubin statistic was less than 1.11 for every jump parameter, measured across the two chains, indicating that the chains are converged. We also estimated the effective sample size

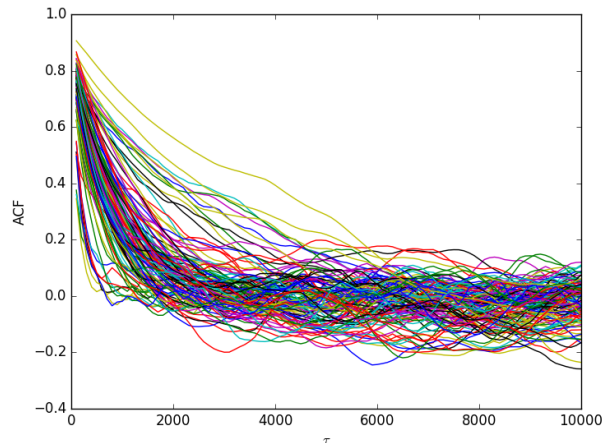


**Figure 2.** Autocorrelation function for all 122 jump parameters versus chain lag,  $\tau$ .

of the chains ( $N_{\text{eff}}$ ) by computing the integrated autocorrelation length as defined in Gelman et al. (2013). We find a minimum  $N_{\text{eff}}$  of 27, with a median value of 118 over all parameters. Fig. 2 shows the autocorrelation function versus time lag for all 122 jump parameters.

The physical parameters of the system were deduced from the jump parameters at each step of the MCMC, so that their posterior PDFs could also be constructed. At each MCMC step, the value for  $R_\star$  was combined with the updated luminosity reported by Van Grootel et al. (2017),  $L_\star = (5.22 \pm 0.19) \times 10^{-4} L_\odot$ , based on their improved measurement of the star’s parallax, to derive a value for  $T_{\text{eff}}$ . For each planet, values for  $R_p$ ,  $a$ , and  $i$ , were deduced from the values for the stellar and transit parameters. Finally, values were also computed for the irradiation of each planet in Earth units and for their equilibrium temperatures, assuming a null Bond albedo.

Fig. 3 shows the detrended period-folded photometry for each planet with the corresponding best-fit transit model, while Figs. B1, B2, B3, B4, and B5 display binned residuals RMS vs. bin size plots for the 78 light curves of our dataset. Figs. B6 and B7 show the cross-correlation plots and histograms of the posterior PDFs derived for the jump parameters of our global analysis, while Table 1 presents the parameters derived for the system. We discuss these results in Section 4.

### 3.3 Stellar variability at $4.5 \mu\text{m}$

Monitoring the stellar variability with *Spitzer* is rendered difficult because of two factors. First, half of the *Spitzer* observations analysed in this paper have been obtained in a time sparse mode, focusing on the transit windows of the seven TRAPPIST-1 planets. These sequences are short, up to four hours long, which is not enough to sample the rotational period of the star. Second, we failed to consistently position the target on the detector’s sweet spot, which systematically affects the measured flux at the  $\sim 2\%$  level. Figure 4 illustrates the absolute flux level measured for all TRAPPIST-1 AORs included in the present paper and the corresponding centroid locations on the detector. Two dis-

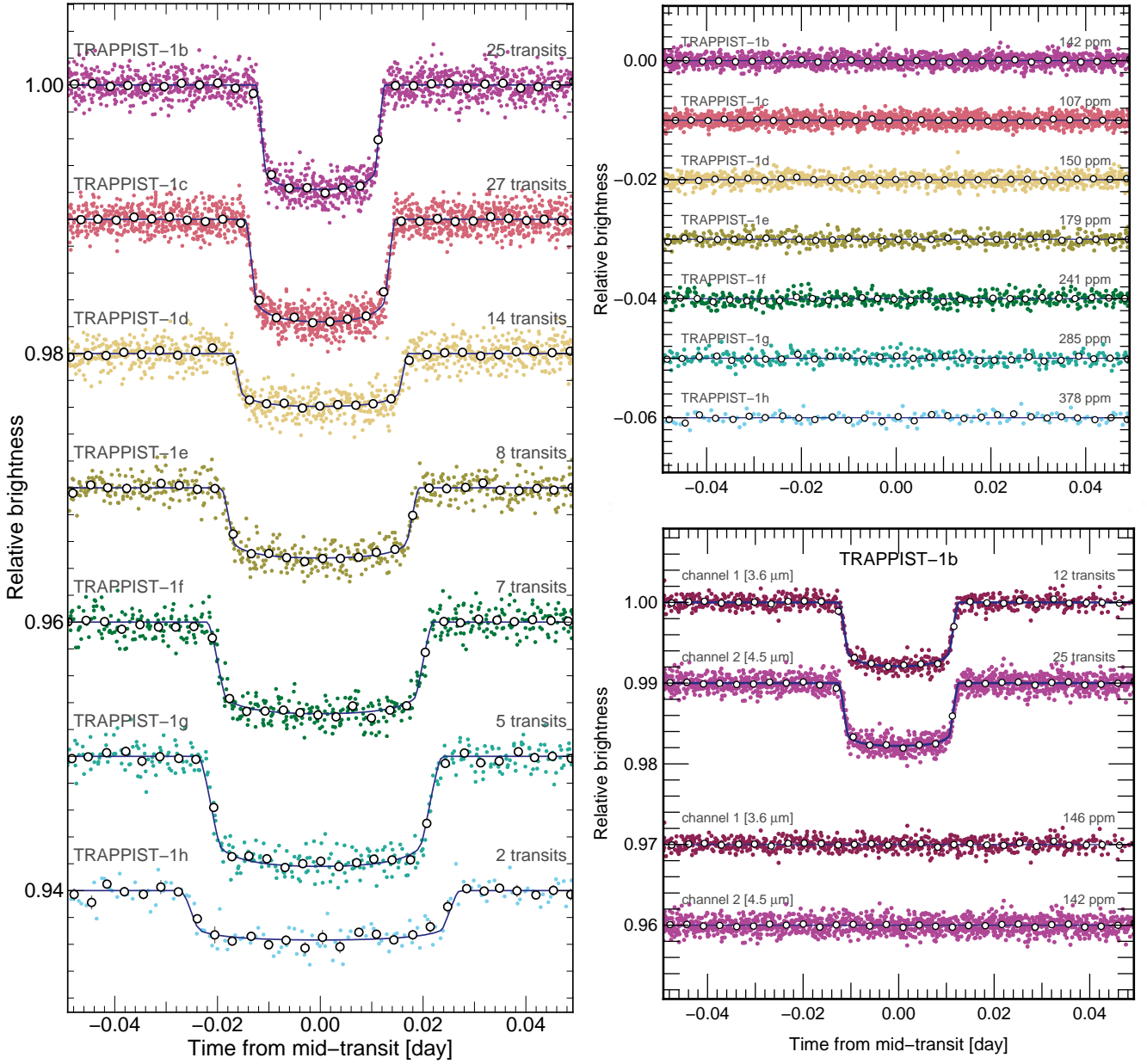


**Figure 3.** *Left:* Period-folded photometric measurements obtained by *Spitzer* at  $4.5\ \mu\text{m}$  near the transits of planets TRAPPIST-1b to TRAPPIST-1h, corrected for the measured TTVs. Coloured dots show the unbinned measurements; open circles depict 5min-binned measurements for visual clarity. The best-fit transit models are shown as coloured lines. The number of transits that were observed to produce these combined curves is written on the plot. *Top right:* Corresponding residuals. The RMS of the residuals (5min bins) is indicated over each planet. *Bottom right:* Similar to other panels, only for TRAPPIST-1b at  $3.6\ \mu\text{m}$  (channel 1) and  $4.5\ \mu\text{m}$  (channel 2).

tinct areas can be seen because of pointing inaccuracies due to the target's large differential parallax between the Earth and *Spitzer*. To mitigate both caveats, we elect to conduct our variability analysis independently from the global fit presented above by only including the quasi-continuous sequence obtained over 21 days in Sept-Oct 2016 (G17). The corresponding centroid locations are clustered on bottom right of Figure 4.

We performed the data reduction by computing the absolute fluxes of all AORs using a fixed aperture size of 3

pixels throughout the dataset. A complication arose from the removal of the pixel-phase effect as TRAPPIST-1 fell 1 to 2 pixels away from the detector's sweet spot for which a high-resolution gain map exists (Ingalls et al. 2016). As no such map was available for our purpose, we calibrated the absolute photometry by using the data itself, using an implementation of the BLISS mapping algorithm (Stevenson et al. 2012). We found that the entire area over which the star fell is relatively extended (0.6 pixels along the  $x$ -axis and 0.5 pixels along the  $y$ -axis), which marginally limits the flux

**Table 1.** Updated system parameters: median values and 1- $\sigma$  limits of the posterior PDFs derived from our global MCMC analysis.

Parameters	Value							
<b>Star</b>								
Mass <sup>a</sup> , $M_\star$ ( $M_\odot$ )	0.0890 ± 0.0070							
Radius, $R_\star$ ( $R_\odot$ )	0.1210 ± 0.0030							
Density, $\rho_\star$ ( $\rho_\odot$ )	51.1 <sup>+1.2</sup> <sub>-2.4</sub>							
Luminosity <sup>a</sup> , $L_\star$ ( $L_\odot$ )	0.000522 ± 0.000019							
Effective temperature, $T_{\text{eff}}$ (K)	2511 ± 37							
Metallicity <sup>a</sup> , [Fe/H] (dex)	+0.04 ± 0.08							
Limb-darkening coefficient <sup>a</sup> , $u_{1,4.5\mu\text{m}}$	0.161 ± 0.019							
Limb-darkening coefficient <sup>a</sup> , $u_{2,4.5\mu\text{m}}$	0.208 ± 0.021							
Limb-darkening coefficient <sup>a</sup> , $u_{1,3.6\mu\text{m}}$	0.168 ± 0.020							
Limb-darkening coefficient <sup>a</sup> , $u_{2,3.6\mu\text{m}}$	0.244 ± 0.021							
<b>Planets</b>								
	<b>b</b>	<b>c</b>	<b>d</b>	<b>e</b>	<b>f</b>	<b>g</b>	<b>h</b>	
Number of transits observed	37	27	14	8	7	5	2	
Period, $P$ (days)	1.51087637	2.42180746	4.049959	6.099043	9.205585	12.354473	18.767953	
	±0.00000039	±0.00000091	±0.000078	±0.000015	±0.000016	±0.000018	±0.000080	
Mid-transit time, $T_0 - 2,450,000$ (BJD <sub>TDB</sub> )	7322.51654	7282.80879	7670.14227	7660.37910	7671.39470	7665.35084	7662.55467	
	±0.00012	±0.00018	±0.00026	±0.00040	±0.00022	±0.00020	±0.00054	
Transit depth at 4.5 $\mu\text{m}$ , $dF_{4.5\mu\text{m}}$ (%)	0.7277 ± 0.0075	0.6940 ± 0.0068	0.3566 ± 0.0070	0.4802 ± 0.0094	0.634 ± 0.010	0.764 ± 0.011	0.346 ± 0.014	
Transit depth at 3.6 $\mu\text{m}$ , $dF_{3.6\mu\text{m}}$ (%)	0.7070 ± 0.0086	-	-	-	-	-	-	
Transit impact parameter, $b$ ( $R_\star$ )	0.157 ± 0.075	0.148 ± 0.088	0.08 <sup>+0.10</sup> <sub>-0.06</sub>	0.240 <sup>+0.056</sup> <sub>-0.047</sub>	0.337 <sup>+0.040</sup> <sub>-0.029</sub>	0.406 <sup>+0.031</sup> <sub>-0.025</sub>	0.392 <sup>+0.039</sup> <sub>-0.043</sub>	
Transit duration, $W$ (min)	36.19 ± 0.12	42.31 ± 0.14	49.33 <sup>+0.43</sup> <sub>-0.32</sub>	55.92 ± 0.39	63.14 ± 0.36	68.53 ± 0.37	76.92 ± 0.96	
Inclination, $i$ (°)	89.56 ± 0.23	89.70 ± 0.18	89.89 <sup>+0.08</sup> <sub>-0.15</sub>	89.736 <sup>+0.053</sup> <sub>-0.066</sub>	89.719 <sup>+0.026</sup> <sub>-0.039</sub>	89.721 <sup>+0.019</sup> <sub>-0.026</sub>	89.796 ± 0.023	
Semi-major axis, $a$ ( $10^{-3}$ AU)	11.50 <sup>+0.28</sup> <sub>-0.25</sub>	15.76 <sup>+0.38</sup> <sub>-0.34</sub>	22.19 <sup>+0.53</sup> <sub>-0.48</sub>	29.16 <sup>+0.70</sup> <sub>-0.63</sub>	38.36 <sup>+0.92</sup> <sub>-0.84</sub>	46.7 ± 1.1	61.7 <sup>+1.5</sup> <sub>-1.3</sub>	
Scale parameter, $a/R_\star$	20.56 <sup>+0.16</sup> <sub>-0.31</sub>	28.16 <sup>+0.22</sup> <sub>-0.44</sub>	39.68 <sup>+0.32</sup> <sub>-0.62</sub>	52.13 <sup>+0.41</sup> <sub>-0.82</sub>	68.6 <sup>+0.6</sup> <sub>-1.1</sub>	83.5 <sup>+0.7</sup> <sub>-1.3</sub>	110.3 <sup>+0.9</sup> <sub>-1.7</sub>	
Irradiation, $S_p$ ( $S_\oplus$ )	3.88 ± 0.22	2.07 ± 0.12	1.043 ± 0.060	0.604 ± 0.034	0.349 ± 0.020	0.236 ± 0.014	0.135 <sup>+0.078</sup> <sub>-0.074</sub>	
Equilibrium temperature <sup>b</sup> $T_{\text{eq}}$ (K)	391.8 ± 5.5	334.8 ± 4.7	282.1 ± 4.0	246.1 ± 3.5	214.5 ± 3.0	194.5 ± 2.7	169.2 ± 2.4	
Radius, $R_p$ ( $R_\oplus$ )	1.127 ± 0.028	1.100 ± 0.028	0.788 ± 0.020	0.915 ± 0.025	1.052 ± 0.026	1.154 ± 0.029	0.777 ± 0.025	

**Notes.** <sup>a</sup> Informative prior PDFs were assumed for these stellar parameters (see Section 3.2).

<sup>b</sup> Assuming a null Bond albedo.

calibration accuracy. For the purposes of this stellar variability analysis, we discarded flares and removed transits based on the parameters deduced from our global analysis (Table 1). The photometric residuals are thus assumed to include signal from the star alone. We measured a photometric residual RMS of 0.11% at a 123-s cadence. We performed a discrete Fourier analysis of the residuals that yielded a maximum at  $\sim 10$  days. The  $3.30 \pm 0.14$ -day rotation period found by Luger et al. (2017a, see also Vida et al. 2017) using 80-day continuous observations of visible K2 data, appears as a low-amplitude peak in our periodogram.

To obtain a more detailed view of the signal components, we further perform a wavelet analysis of the photometric residuals. For this purpose, we use the weighted wavelet Z-transform (WWZ) code presented in Foster (1996). The wavelet Z-statistic is computed as a function of both time and frequency, which gives further insights into the structure of the photometric residuals. The results of this analysis are shown on Figure 5. We find that multiple peaks exist but that are of low amplitude. No signal is apparent around 3.3 days but the  $\sim 10$ -day signature seems to

persist across the entire window, albeit of low significance. The low-amplitude residual correlated noise could originate from imperfect instrumental systematic correction or from stellar noise. Assuming that the systematics correction we use is efficient, the wavelet analysis applied to the photometric residuals suggests that the star exhibits multiple active regions that evolve rapidly with time. The data at hand does not enable us to clearly identify the structure of the signal. We argue that long-term parallel monitoring of TRAPPIST-1 in the visible and infrared are desirable to better constrain its variability patterns.

We carried out an additional analysis of the power spectrum of TRAPPIST-1 using a correlated noise model described by a Gaussian process with a power spectrum defined as the sum of stochastically-driven damped simple-harmonic oscillators, each with quality factor  $Q$  and frequency  $\omega_0$  (Foreman-Mackey et al. 2017). We fit the data with two components: a fixed  $Q = 1/\sqrt{2}$  term which has a power spectrum describing variability similar to granulation, and a second  $Q \gg 1$  term describing (quasi-)periodic variability, with a frequency initialized for a period of 3 days.

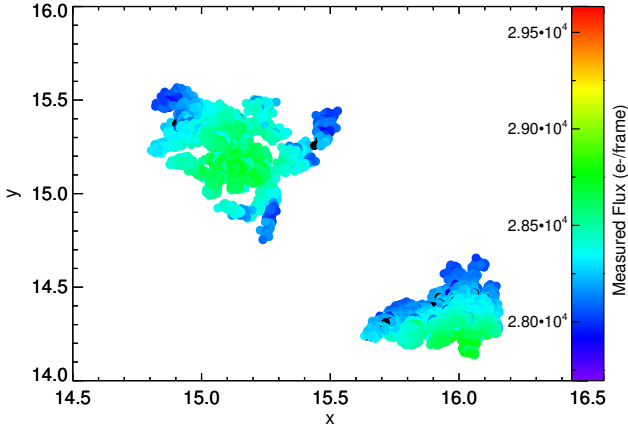


**Figure 4.** TRAPPIST-1 *Spitzer*/IRAC raw photometric fluxes collected from all 66 AORs taken between 2016 and March 2017 and the corresponding centroid locations on the detector.

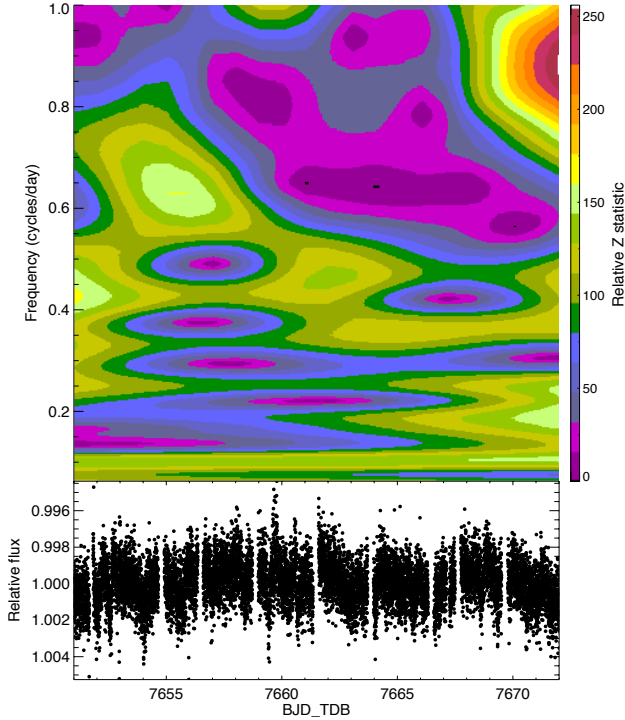


**Figure 5.** Wavelet diagram (*top*) of the photometric residuals (*bottom*).

We found that the amplitude of the large- $Q$  term decreased to zero when optimizing the parameters of the Gaussian process, indicating that there is no evidence for quasi-periodic variability in the *Spitzer* 4.5- $\mu\text{m}$  dataset. We found that the “granulation” term had a finite amplitude with a variance of  $7 \times 10^{-4}$ , and a frequency  $\omega_0 = 22.45 \text{ rad day}^{-1}$ , corresponding to a characteristic damping timescale of 0.28 days. Once the power spectrum was optimized, we subtracted off the Gaussian process estimate of the correlated noise component, and found that the normalized residuals follow a Gaussian, but slightly broader by a factor of 1.065, which is an additional argument for increasing the uncertainties on the data points with the correction factors,  $CF$ , as discussed above.

## 4 DISCUSSION

### 4.1 Updated system parameters

We have more than doubled the number of transit events observed with *Spitzer* on TRAPPIST-1 with respect to what has been presented in G17. Our global analysis refines the planets’ transit depths (at 4.5  $\mu\text{m}$ ) by factors up to 2.8 (TRAPPIST-1e) and their transit durations by factors up to 2.8 (TRAPPIST-1h), and also slightly improves the precision of the physical parameters derived for the planets. An important point to outline is that in G16 and G17 our global analysis assumed an informative prior on the stellar mass and radius - and thus on the stellar density - based on stellar evolution models. In this new analysis, no informative prior was assumed for the stellar radius, and the stellar density was only constrained by the shape of the transits of the seven planets (Seager & Mallén-Ornelas 2003). Furthermore, our assumed prior on the stellar mass was here not only based on stellar physics computations but also on empirical data (see Section 3.2 and Van Grootel et al. 2017). We thus consider our updated planetary parameters presented in Table 1 not only more precise than those reported in G17, but also more accurate because they are less model-dependent. We compare some of these quantities to Solar system objects and the rest of the small exoplanet population in Fig. 6.

### 4.2 Variability of the transit parameters

As reported in Section 3.3, we do not find any significant (quasi-)periodic signal in the IRAC 4.5- $\mu\text{m}$  band related to the rotation of TRAPPIST-1. Rotational variability has however been previously detected by Luger et al. (2017a) in the  $K2$  passband, at the level of few percents and with a period of  $\sim 3.3$  days. This periodic photometric variability indicates that inhomogeneities of the stellar surface (spots) move in and out of view as the star rotates. Luger et al. (2017b) recently demonstrated that the orbital planes of the TRAPPIST-1 planets are aligned to  $< 0.3^\circ$  at 90% confidence. Together, the planets cover at least 56% of a hemisphere when they transit (shaded area in Fig. 7), notably the low and intermediate latitudes at which we find spots on the Sun (e.g. Miletskii & Ivanov 2009). We could therefore expect the planets to cross some stellar spots during their transits. Such occulted spots would affect the transit profile in a way that would depend on their size, contrast, and distribution across the planetary chord, and would tend to make the transit shallower. Unocculted spots, i.e., stellar spots that are not crossed during planetary transits, would have the opposite effect, making the transit deeper by diminishing the overall flux from the star while leaving the surface brightness along the transit chord unchanged. Because of stellar spots, either occulted or unocculted, we could thus expect to detect variations in the planets’ transit depths as a function of time.

As noted in Section 3.1, the transit depths derived from the individual analyses generally follow a normal distribution for each planet, except TRAPPIST-1b at 3.6  $\mu\text{m}$ , TRAPPIST-1e, and TRAPPIST-1g, each of which show some outliers. It is common knowledge that transit parameters derived from a single transit light curve can be significantly affected by systematics (e.g. Gillon et al. 2012). The



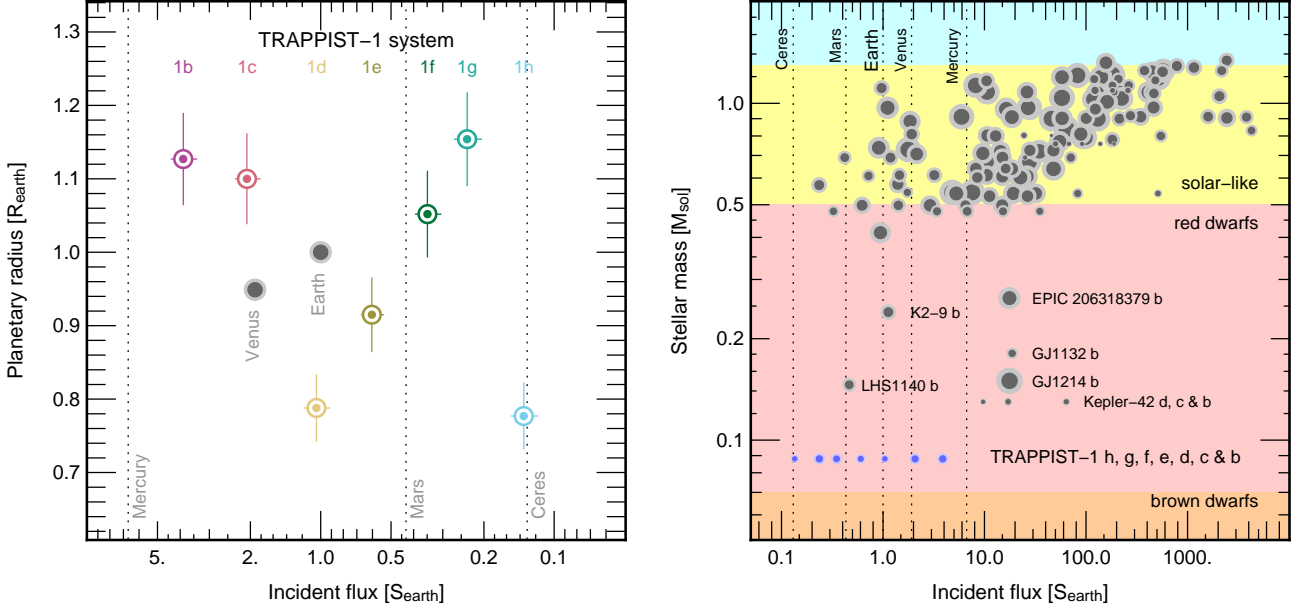


**Figure 6.** Updates on diagrams shown in G16 and G17. *Left:* Planetary radii as a function of incident flux. *Right:* Planet population shown ordered by stellar-host mass as a function of incident flux. Only planets with radii  $< 2R_{\oplus}$  are represented. The dots size increases linearly with radius.

global analysis of an extensive set of transit light curves, which assumes one unique transit profile for all the transit light curves (of a same planet), allows a better separation of the actual transit signal from the correlated noise and the derivation of robust transit parameters. To better assess the possible variations in the transit depth of each planet, we computed for each of its transits the median values of the photometric residuals in transit and out of transit, using for this purpose the photometric residuals from the global analysis. These median values, together with the median absolute deviations, are given for each transit in Table B1. A significant difference between the in-transit and out-of-transit medians of the photometric residuals for a given transit would indicate a variation in its depth compared to the planet’s transit depth derived from the global analysis. However, the in-transit and out-of-transit medians are compatible within 1 sigma for all transits of all planets. This test reveals that the variability seen for some planets (TRAPPIST-1b at  $3.6 \mu\text{m}$ , TRAPPIST-1e, and TRAPPIST-1g) in the transit depths derived from the individual analyses is likely not physical but rather caused by systematic effects –which are better disentangled from the planetary signals in the global analysis.

In this context, it is worth noting that instrumental systematics are stronger at  $3.6 \mu\text{m}$  than at  $4.5 \mu\text{m}$  and thus require more complex baseline models, which can introduce some biases in the transit parameters derived from a single light curve. This might explain the increased scatter of TRAPPIST-1b’s individual transit depths at  $3.6 \mu\text{m}$ . For TRAPPIST-1e, we note that only the first transit in Fig. 1 (epoch -1) shows a discrepant transit depth. This transit was actually observed over two different consecutive AORs, which might have introduced a bias in its measured depth.

As for TRAPPIST-1g, a visual inspection of the global analysis’ residuals for the two transits with discrepant transit depths (second and fifth transits in Fig. 1, corresponding to epochs 0 and 14 respectively) does not reveal any obvious structures or spot-crossings. The origin of these two outliers thus remains unclear. Additional transit observations of this planet at higher SNR are needed to better assess the possible variability of its transit depth.

Overall, *Spitzer* transits of TRAPPIST-1 planets thus appear to be mostly immune to the effects of stellar variability. There are several reasons why this may happen:

- Considering the very low level of low-frequency photometric variability shown by TRAPPIST-1 at  $4.5 \mu\text{m}$ , unocculted spots may not have a significant impact on the planets’ transit depths. Using the simple model of Berta et al. (2011, see their Equations 8 and 9) to estimate the expected amplitude of transit depth variations at  $4.5 \mu\text{m}$  due to unocculted spots based on the stellar variability measured in that band, we indeed find amplitudes lower than 100 ppm for all the planets. This is smaller than the error bars on the individual transit depths. We note however that this estimate is only a lower limit to the possible amplitude of transit depth variations due to unocculted spots. Indeed, the rotational variability of the star reflects only the non-axisymmetric component of the stellar surface inhomogeneities. The axisymmetric component does not contribute to the measured stellar variability and its effect is thus not included in our estimate, while it is also expected to affect the planets’ transit depths.

- The periodic variability detected in the *K2* passband may be caused by high-latitude spots that do not cross the planets’ chords, explaining the non-detection of spot-crossing events. Evidence for such high-latitude spots has

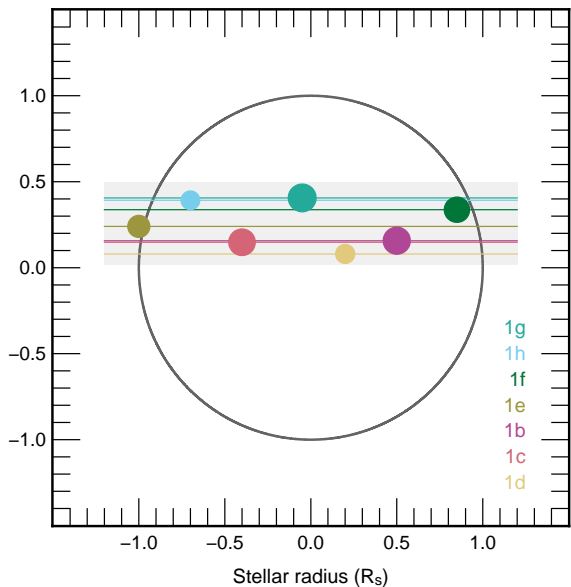


**Figure 7.** Representation of the star, and of the planets that transit it, using impact parameters and transit depths from Table 1. The planets cover a minimum area of  $\sim 56\%$  of an hemisphere. Planetary position on its chord is arbitrary.

been reported for some mid- and late-M dwarfs (see e.g. Barnes et al. 2015). We note however that these objects are usually young ( $\lesssim 1$  Gyr), while TRAPPIST-1 is a rather old system ( $7.6 \pm 2.2$  Gyr, Burgasser & Mamajek 2017).

- Spot-crossing events may not produce detectable effects on the *Spitzer* transit light curves due to the reduced spot-to-photosphere contrast in the IRAC passbands (see e.g. Ballerini et al. 2012). A practical example of this effect was presented by Fraine et al. (2014), who reported simultaneous *Kepler* and *Spitzer* transit photometry of the Neptune-sized planet HAT-P-11b orbiting an active K4 dwarf. While some spot-crossing events are clearly visible in the *Kepler* optical photometry, they are undetected in the photometry obtained concurrently with *Spitzer* at  $4.5 \mu\text{m}$ .

### 4.3 Transmission spectrum of TRAPPIST-1b

A transmission spectrum can be severely affected by both occulted and unocculted stellar spots (e.g. Jordán et al. 2013; McCullough et al. 2014; Rackham et al. 2017). To extract a proper transmission spectrum, a planet needs to cover a part of the stellar surface that has a spectrum that is representative of the whole disc. We are in a privileged position with TRAPPIST-1 as the planets cross over a quarter of the entire stellar surface, and more than half of a hemisphere. Unless spots never intersect transit chords, the planets will cross over a representative fraction of the star, and the transmission spectra measured for the TRAPPIST-1 planets should be robust measures of their atmospheres (de Wit et al. 2016; Barstow & Irwin 2016; Morley et al. 2017).

Our global data analysis yields a marginal transit depth difference of  $+208 \pm 110$  ppm for TRAPPIST-1b between the *Spitzer*/IRAC  $4.5\text{-}\mu\text{m}$  and  $3.6\text{-}\mu\text{m}$  channels, the tran-

sit being slightly deeper at  $4.5 \mu\text{m}$  than at  $3.6 \mu\text{m}$  (Table 1). If confirmed, this transit depth variation would imply that TRAPPIST-1b’s atmosphere significantly exceeds its equilibrium temperature (392 K assuming a null Bond albedo, Table 1). A deeper transit depth at  $4.5 \mu\text{m}$  would be best explained by atmospheric  $\text{CO}_2$ , which has a prominent absorption feature around  $4.2 \mu\text{m}$  (see e.g., Kaltenegger & Traub 2009). The most favorable scenario to enhance such a signature requires no other opacity source across the IRAC  $3.6\text{-}\mu\text{m}$  channel than the extended wing of the  $4.2\text{-}\mu\text{m}$  absorption band of  $\text{CO}_2$ . In such a case, the variation in transit depth is approximately equivalent to 5 scale heights ( $H$ ) at medium spectral resolution (see e.g., Kaltenegger & Traub 2009; de Wit & Seager 2013) and  $2H$  when binned over IRAC’s channels. TRAPPIST-1b’s scale height would thus be larger or equal to approximately 52 km ( $208 \text{ ppm} = ((R_p + 2H)/R_\star)^2 - (R_p/R_\star)^2$ ). For comparison, the Earth’s atmospheric scale height is 8.5 km, while that of Venus is 15.9 km<sup>3</sup>. This lower limit on the planet atmospheric scale height can be translated into a lower limit on its atmospheric temperature owing to assumptions of its atmospheric mean molecular mass,  $\mu$ , and surface gravity,  $g$ . Planet b’s surface gravity is approximately  $8 \text{ m/s}^2$  (Grimm et al. 2017). Under the present assumption that no strong absorber affects the  $3.6\text{-}\mu\text{m}$  band, the background gas cannot be water or methane—both exhibit absorption features in this band—implying that the atmosphere must have a large  $\mu$  (e.g., 28 u.m.a. if dominated by  $\text{N}_2$ ). Under such a favorable scenario for the  $\text{CO}_2$  feature, TRAPPIST-1 b’s atmosphere would require an average temperature above 1400 K—more than three times larger than its estimated equilibrium temperature. On the other hand, if water dominates its atmosphere, this would lead to two counter-balancing effects: (1) a decrease of the mean molecular weight and (2) a transit depth variation between the two IRAC channels of no more than a scale height due to water absorption at  $3.3 \mu\text{m}$ . This would yield an atmospheric scale height larger than  $\sim 100$  km and an average atmospheric temperature above  $\sim 1800$  K. Other opacity sources, such as clouds or hazes, would require an even larger scale height and atmospheric temperature to support such a variation in transit depth between the two IRAC channels. Therefore, if confirmed, such hint of variability would be indicative of a surprisingly large atmospheric temperature for TRAPPIST-1b.

As demonstrated recently by Deming & Sheppard (2017), transit measurements of a planet transiting an M-dwarf can be affected by a resolution-linked bias (RLB) effect, which acts to decrease the apparent amplitude of an absorption feature from the planetary atmosphere. This is due to the complex line structure exhibited by M-dwarfs which creates a flux-leakage effect at low to medium spectral resolution wherein the stellar flux does not entirely cancel out in the ratio of in- to out-of-transit flux. We estimated the amplitude of the RLB effect on the transit depth difference expected for TRAPPIST-1b between the IRAC  $4.5\text{-}\mu\text{m}$  and  $3.6\text{-}\mu\text{m}$  channels assuming different atmospheric scenarios, namely  $\text{H}_2$ -,  $\text{H}_2\text{O}$ -,  $\text{N}_2$ -, and  $\text{CO}_2$ -rich atmospheres (de Wit et al. 2016). For TRAPPIST-1 spectrum, we used the PHOENIX/BT-Settl model with  $T_{\text{eff}}/\log g/[M/H]$  of

<sup>3</sup> <https://nssdc.gsfc.nasa.gov/planetary/factsheet/>

2500K/5.5/0.0 (Allard et al. 2012). We find a maximal RLB effect of  $\sim 115$  ppm over a  $\sim 2400$  ppm absorption feature of methane in a  $\text{H}_2$ -rich atmosphere, which corresponds to a dampening of the methane absorption feature by  $\sim 5\%$ . Although the amplitude of the effect in this case is comparable to the uncertainty on our measured transit depth difference, it is not relevant for the interpretation of our measurements as the hint of feature detected between the two IRAC channels is not of the order of  $\sim 2400$  ppm. We find amplitudes ranging from only a few ppm to 30 ppm for the other atmospheric scenarios. The marginal difference in transit depth that we measure between both IRAC bands is thus not expected to be significantly affected by the RLB effect.

## 5 CONCLUSIONS

In this work, we presented 60 new transits of the TRAPPIST-1 planets observed with *Spitzer*/IRAC in early 2017. We performed a global analysis of the entire *Spitzer* dataset gathered so far, which enabled us to refine the transit parameters and to provide revised values for the planets' physical parameters, notably their radii, using updated properties for the host star. As part of this study, we also extracted precise transit timings that will be instrumental for TTV studies of the system, to be presented in a companion paper. In addition, we found that the star shows a very low level of low-frequency variability in the IRAC  $4.5\text{-}\mu\text{m}$  channel. We did not detect any evidence of a (quasi-)periodic signal related to stellar rotation and found that the planets' transit depths measured with *Spitzer* are mostly not affected by stellar variability. Finally, we also found for TRAPPIST-1b a marginal transit depth difference of  $+208 \pm 110$  ppm between the IRAC  $4.5\text{-}\mu\text{m}$  and  $3.6\text{-}\mu\text{m}$  channels. If confirmed, this transit depth variation could indicate the presence of  $\text{CO}_2$  in the planet's atmosphere as well as a surprisingly large atmospheric temperature. Together, these results improve our understanding of this remarkable system and help prepare the detailed atmospheric characterization of its planets with JWST.

## ACKNOWLEDGEMENTS

We thank E. Gillen for interesting discussions and valuable suggestions. This work is based in part on observations made with the *Spitzer* Space Telescope, which is operated by the Jet Propulsion Laboratory, California Institute of Technology, under a contract with NASA. This work was partially supported by a grant from the Simons Foundation (PI Queloz, grant number 327127). The research leading to these results also received funding from the European Research Council (ERC) under the FP/2007-2013 ERC grant agreement no. 336480, and under the H2020 ERC grant agreement no. 679030; and from an Action de Recherche Concertée (ARC) grant, financed by the Wallonia-Brussels Federation. L.D. acknowledges support from the Gruber Foundation Fellowship. V.V.G. and M.G. are F.R.S.-FNRS Research Associates. E.J. is F.R.S.-FNRS Senior Research Associate. B.-O.D. acknowledges support from the Swiss National Science Foundation in the form of a SNSF Professorship (PP00P2\_163967). E.B. acknowledges funding by

the European Research Council through ERC grant SPIRE 647383. A.J.B. acknowledges funding support from the US-UK Fulbright Scholarship program.

## REFERENCES

- Agol E., Steffen J., Sari R., Clarkson W., 2005, *MNRAS*, **359**, 567  
Allard F., Homeier D., Freytag B., 2012, *Philosophical Transactions of the Royal Society of London Series A*, **370**, 2765  
Ballerini P., Micela G., Lanza A. F., Pagano I., 2012, *A&A*, **539**, A140  
Barnes J. R., Jeffers S. V., Jones H. R. A., Pavlenko Y. V., Jenkins J. S., Haswell C. A., Lohr M. E., 2015, *ApJ*, **812**, 42  
Barstow J. K., Irwin P. G. J., 2016, *MNRAS*, **461**, L92  
Berta Z. K., Charbonneau D., Bean J., Irwin J., Burke C. J., Désert J.-M., Nutzman P., Falco E. E., 2011, *ApJ*, **736**, 12  
Bolmont E., Selsis F., Owen J. E., Ribas I., Raymond S. N., Leconte J., Gillon M., 2017, *MNRAS*, **464**, 3728  
Bonfils X., et al., 2013, *A&A*, **549**, A109  
Bourrier V., et al., 2017, *A&A*, **599**, L3  
Burgasser A. J., Mamajek E. E., 2017, *ApJ*, **845**, 110  
Chabrier G., 2003, *PASP*, **115**, 763  
Claret A., Bloemen S., 2011, *A&A*, **529**, A75  
Cubillos P., Harrington J., Loredo T. J., Lust N. B., Bleicic J., Stemm M., 2017, *AJ*, **153**, 3  
Deming D., Sheppard K., 2017, *ApJ*, **841**, L3  
Demory B.-O., Gillon M., Madhusudhan N., Queloz D., 2016, *MNRAS*, **455**, 2018  
Dressing C. D., Charbonneau D., 2013, *ApJ*, **767**, 95  
Dressing C. D., Charbonneau D., 2015, *ApJ*, **807**, 45  
Dupuy T. J., Liu M. C., 2017, *ApJS*, **231**, 15  
Eastman J., Siverd R., Gaudi B. S., 2010, *PASP*, **122**, 935  
Fazio G. G., et al., 2004, *ApJS*, **154**, 10  
Foreman-Mackey D., 2016, *The Journal of Open Source Software*, **24**  
Foreman-Mackey D., Agol E., Ambikasaran S., Angus R., 2017, *AJ*, **154**, 220  
Foster G., 1996, *AJ*, **112**, 1709  
Fraire J., et al., 2014, *Nature*, **513**, 526  
Gelman A., Rubin D. B., 1992, *Statistical Science*, **7**, 457  
Gelman A., Carlin J., Stern H., Dunson D., Vehtari A., Rubin D., 2013, *Bayesian Data Analysis*, Third Edition. Chapman & Hall/CRC Texts in Statistical Science, Taylor & Francis, <https://books.google.fr/books?id=ZXL6AQAQBAJ>  
Gillon M., et al., 2012, *A&A*, **542**, A4  
Gillon M., et al., 2014, *A&A*, **563**, A21  
Gillon M., et al., 2016, *Nature*, **533**, 221  
Gillon M., et al., 2017, *Nature*, **542**, 456  
Grimm S., et al., 2017, submitted to *A&A*  
He M. Y., Triaud A. H. M. J., Gillon M., 2017, *MNRAS*, **464**, 2687  
Henry T. J., Jao W.-C., Subasavage J. P., Beaulieu T. D., Ianna P. A., Costa E., Méndez R. A., 2006, *AJ*, **132**, 2360  
Holman M. J., Murray N. W., 2005, *Science*, **307**, 1288  
Ingalls J. G., Krick J. E., Carey S. J., Laine S., Surace J. A., Glaccum W. J., Grillmair C. C., Lowrance P. J., 2012, in *Space Telescopes and Instrumentation 2012: Optical, Infrared, and Millimeter Wave*. p. 84421Y, doi:10.1117/12.926947  
Ingalls J. G., et al., 2016, *AJ*, **152**, 44  
Jordán A., et al., 2013, *ApJ*, **778**, 184  
Kaltenegger L., Traub W. A., 2009, *ApJ*, **698**, 519  
Knutson H. A., Charbonneau D., Allen L. E., Burrows A., Megeath S. T., 2008, *ApJ*, **673**, 526  
Kroupa P., 2001, *MNRAS*, **322**, 231  
Lanotte A. A., et al., 2014, *A&A*, **572**, A73  
Luger R., et al., 2017a, preprint, (arXiv:1703.04166)

- Luger R., Lustig-Yaeger J., Agol E., 2017b, preprint, ([arXiv:1711.05739](#))
- MacDonald J., Mullan D. J., 2014, *ApJ*, **787**, 70
- Mandel K., Agol E., 2002, *ApJ*, **580**, L171
- McCullough P. R., Crouzet N., Deming D., Madhusudhan N., 2014, *ApJ*, **791**, 55
- Miletskii E. V., Ivanov V. G., 2009, *Astronomy Reports*, **53**, 857
- Morley C. V., Kreidberg L., Rustamkulov Z., Robinson T., Fortney J. J., 2017, preprint, ([arXiv:1708.04239](#))
- Nutzman P., Charbonneau D., 2008, *PASP*, **120**, 317
- O'Malley-James J. T., Kaltenegger L., 2017, *MNRAS*, **469**, L26
- Rackham B., et al., 2017, *ApJ*, **834**, 151
- Schwarz G., 1978, *Annals of Statistics*, **6**, 461
- Seager S., Mallén-Ornelas G., 2003, *ApJ*, **585**, 1038
- Stetson P. B., 1987, *PASP*, **99**, 191
- Stevenson K. B., et al., 2012, *ApJ*, **754**, 136
- Tamayo D., et al., 2016, *ApJ*, **832**, L22
- Tamayo D., Rein H., Petrovich C., Murray N., 2017, *ApJ*, **840**, L19
- Torres G., 2013, *Astronomische Nachrichten*, **334**, 4
- Van Grootel V., et al., 2017, preprint, ([arXiv:1712.01911](#))
- Vida K., Kóvári Z., Pál A., Oláh K., Kriskovics L., 2017, *ApJ*, **841**, 124
- Wheatley P. J., Loudon T., Bourrier V., Ehrenreich D., Gillon M., 2017, *MNRAS*, **465**, L74
- Winn J. N., et al., 2008, *ApJ*, **683**, 1076
- Wordsworth R., Pierrehumbert R., 2014, *ApJ*, **785**, L20
- de Wit J., Seager S., 2013, *Science*, **342**, 1473
- de Wit J., et al., 2016, *Nature*, **537**, 69

## APPENDIX A: RESULTS FROM THE INDIVIDUAL ANALYSES

Table A1: Median values and 1- $\sigma$  limits of the posterior PDFs deduced for the timings, depths, and durations of the transits from their individual analyses.

Planet	Epoch	Channel	$T_0$	$eT_0$	$dF$	$edF$	$W$	$eW$
			[BJD <sub>TDB</sub> - 2450000]		[%]		[min]	
b	78	2	7440.36514	0.00035	0.742	0.048	36.30	1.20
	86	2	7452.45228	0.00014	0.757	0.025	35.76	0.40
	93	2	7463.02847	0.00019	0.682	0.025	36.68	0.59
	218	2	7651.88743	0.00022	0.774	0.040	36.36	0.69
	219	2	7653.39809	0.00026	0.684	0.031	36.19	0.68
	220	2	7654.90908	0.00084	0.759	0.024	35.80	2.20
	222	2	7657.93129	0.00020	0.735	0.030	36.26	0.54
	223	2	7659.44144	0.00017	0.746	0.029	36.84	0.58
	224	2	7660.95205	0.00033	0.675	0.041	37.07	0.95
	225	2	7662.46358	0.00020	0.757	0.036	36.39	0.60
	226	2	7663.97492	0.00070	0.776	0.045	35.90	1.90
	227	2	7665.48509	0.00017	0.772	0.032	36.45	0.50
	228	2	7666.99567	0.00025	0.704	0.043	36.10	0.81
	229	2	7668.50668	0.00030	0.728	0.041	36.54	0.81
	230	2	7670.01766	0.00034	0.751	0.048	36.75	0.89
	231	2	7671.52876	0.00030	0.702	0.045	36.78	0.86
	318	2	7802.97557	0.00016	0.751	0.027	35.73	0.65
	320	2	7805.99697	0.00016	0.699	0.023	36.29	0.50
	321	2	7807.50731	0.00017	0.703	0.026	36.75	0.52
	322	1	7809.01822	0.00017	0.801	0.028	36.01	0.65
	324	2	7812.04038	0.00020	0.703	0.027	36.64	0.59
	325	2	7813.55121	0.00014	0.732	0.022	36.43	0.43
	326	1	7815.06275	0.00017	0.724	0.023	36.76	0.53
	327	1	7816.57335	0.00011	0.663	0.021	35.36	0.35
	328	2	7818.08382	0.00015	0.723	0.026	36.41	0.46
	329	1	7819.59478	0.00017	0.704	0.028	36.21	0.53
	330	1	7821.10550	0.00020	0.737	0.032	36.33	0.60
	332	2	7824.12730	0.00018	0.737	0.029	36.29	0.55
	333	1	7825.63813	0.00018	0.706	0.033	36.19	0.60
	334	1	7827.14995	0.00012	0.742	0.023	36.33	0.42
	335	1	7828.66042	0.00024	0.727	0.031	35.70	0.69
	336	2	7830.17087	0.00021	0.708	0.032	36.44	0.60
	338	1	7833.19257	0.00018	0.618	0.023	35.67	0.55
	339	1	7834.70398	0.00016	0.682	0.020	37.14	0.49
340	2	7836.21440	0.00017	0.706	0.028	35.59	0.50	
341	1	7837.72526	0.00014	0.702	0.023	35.74	0.56	
342	1	7839.23669	0.00017	0.808	0.025	35.76	0.56	
c	70	2	7452.33470	0.00015	0.698	0.023	42.28	0.48
	71	2	7454.75672	0.00066	0.644	0.037	42.60	2.00
	152	2	7650.92395	0.00023	0.708	0.029	43.59	0.79
	153	2	7653.34553	0.00024	0.668	0.026	42.62	0.69
	154	2	7655.76785	0.00040	0.679	0.050	43.10	1.00
	155	2	7658.18963	0.00024	0.668	0.030	42.11	0.66
	156	2	7660.61168	0.00051	0.681	0.056	42.20	1.30
	157	2	7663.03292	0.00028	0.710	0.031	42.46	0.88
	158	2	7665.45519	0.00025	0.719	0.030	42.18	0.65
	159	2	7667.87729	0.00031	0.700	0.038	42.54	0.81
	160	2	7670.29869	0.00035	0.731	0.044	42.34	0.96
	215	2	7803.49747	0.00020	0.672	0.025	41.42	0.59
	216	2	7805.91882	0.00017	0.652	0.020	42.21	0.48
	217	2	7808.34123	0.00023	0.735	0.035	41.98	0.71
	218	2	7810.76273	0.00019	0.674	0.029	42.45	0.62
219	2	7813.18456	0.00024	0.668	0.024	42.02	0.72	
220	2	7815.60583	0.00017	0.725	0.024	42.88	0.55	
221	2	7818.02821	0.00020	0.763	0.024	42.28	0.53	
222	2	7820.45019	0.00022	0.674	0.024	41.76	0.60	

*Continued on next page*

Table A1 – *continued from previous page*

Planet	Epoch	Channel	$T_0$ [BJD <sub>TDB</sub> – 2450000]	$eT_0$	$dF$ [%]	$edF$	$W$ [min]	$eW$
	223	2	7822.87188	0.00021	0.756	0.028	42.67	0.66
	224	2	7825.29388	0.00022	0.672	0.025	42.12	0.66
	225	2	7827.71513	0.00022	0.718	0.029	42.21	0.62
	226	2	7830.13713	0.00026	0.705	0.033	42.90	0.79
	227	2	7832.55888	0.00015	0.732	0.026	42.95	0.49
	228	2	7834.98120	0.00025	0.673	0.030	42.56	0.81
	229	2	7837.40280	0.00017	0.697	0.024	41.98	0.52
	230	2	7839.82415	0.00031	0.679	0.063	42.05	0.86
d	-4	2	7653.94261	0.00051	0.390	0.038	49.00	2.20
	-3	2	7657.99220	0.00063	0.333	0.027	49.20	1.90
	-2	2	7662.04284	0.00051	0.395	0.030	50.10	1.50
	-1	2	7666.09140	0.00130	0.308	0.043	48.90	2.80
	0	2	7670.14198	0.00066	0.366	0.045	49.00	1.60
	33	2	7803.79083	0.00049	0.366	0.021	49.40	1.30
	34	2	7807.84032	0.00030	0.384	0.020	49.39	0.91
	35	2	7811.89116	0.00050	0.382	0.024	48.60	1.40
	36	2	7815.94064	0.00030	0.348	0.019	50.21	0.85
	37	2	7819.99050	0.00050	0.312	0.021	49.80	1.40
	38	2	7824.04185	0.00067	0.383	0.025	49.20	1.50
	39	2	7828.09082	0.00043	0.387	0.031	49.40	1.10
	40	2	7832.14036	0.00037	0.331	0.023	48.90	1.10
	41	2	7836.19171	0.00042	0.345	0.023	48.80	1.10
e	-1	2	7654.27862	0.00049	0.582	0.043	58.60	1.40
	0	2	7660.38016	0.00078	0.495	0.047	56.40	1.90
	24	2	7806.75758	0.00041	0.439	0.027	55.70	1.20
	25	2	7812.85701	0.00034	0.449	0.023	55.10	1.00
	26	2	7818.95510	0.00030	0.482	0.022	56.07	0.92
	27	2	7825.05308	0.00035	0.432	0.024	55.44	0.96
	28	2	7831.15206	0.00027	0.516	0.018	56.19	0.85
	29	2	7837.24980	0.00025	0.499	0.021	55.58	0.71
f	-2	2	7652.98579	0.00032	0.658	0.020	65.90	1.40
	-1	2	7662.18747	0.00040	0.620	0.037	65.30	1.80
	0	2	7671.39279	0.00072	0.692	0.070	64.70	4.00
	15	2	7809.47554	0.00027	0.648	0.025	63.47	0.82
	16	2	7818.68271	0.00032	0.634	0.022	63.35	0.93
	17	2	7827.88669	0.00030	0.628	0.024	63.11	0.86
	18	2	7837.10322	0.00032	0.610	0.023	63.36	0.95
g	-1	2	7652.99481	0.00030	0.817	0.028	68.60	1.00
	0	2	7665.35151	0.00028	0.691	0.026	67.49	0.82
	12	2	7813.60684	0.00023	0.777	0.020	68.88	0.72
	13	2	7825.96112	0.00020	0.793	0.019	68.30	0.79
	14	2	7838.30655	0.00028	0.695	0.026	68.08	0.98
h	0	2	7662.55467	0.00054	0.348	0.024	76.1	2.1
	9	2	7831.46625	0.00047	0.346	0.016	77.2	1.3

## APPENDIX B: GLOBAL ANALYSIS: SUPPLEMENTARY MATERIAL

### B1 Binned residuals RMS vs. bin size plots

Figs. B1, B2, B3, B4, and B5 show the RMS vs. bin size plots for the 78 *Spitzer*/IRAC light curves of our dataset, made using the `binrms` routine of the `MC3` open-source Python package (Cubillos et al. 2017). For each light curve, the RMS of the binned residuals,  $\text{RMS}_N$ , is shown as a black curve for bin sizes (i.e. the mean number  $N$  of points in each bin) ranging from one to half the data size. The uncertainty of  $\text{RMS}_N$  (grey error bars) is computed as  $\sigma_{\text{RMS}} = \text{RMS}_N / \sqrt{2M}$  (see Cubillos et al. 2017 for the derivation), where  $M$  is the number of bins. The red curve shows the expected RMS  $\sigma_N$  in the absence of correlated noise, given by (Winn et al. 2008):

$$\sigma_N = \frac{\sigma_1}{\sqrt{N}} \sqrt{\frac{M}{M-1}} \quad (\text{B1})$$

where  $\sigma_1$  is the RMS of the unbinned residuals. The saw-tooth look of this red curve arises from the discrete change in  $M$ , which becomes more significant as  $N$  increases.

As mentioned in Section 3, the possible presence of correlated noise in the data is accounted for in our analyses via correction factors  $CF$  that we applied to the photometric error bars of each light curve before performing the final analyses. For each light curve,  $CF$  is the product of two contributions,  $\beta_w$  and  $\beta_r$ . On one side,  $\beta_w$  represents the under- or overestimation of the white noise of each measurement. It is computed as the ratio between the RMS of the unbinned residuals and the mean photometric error. On the other side,  $\beta_r$  allows to account for possible correlated noise present in the light curve, and is calculated as:

$$\beta_r = \frac{\text{RMS}_N}{\sigma_N} \quad (\text{B2})$$

$$= \frac{\sigma_N}{\sigma_1} \sqrt{\frac{N(M-1)}{M}} \quad (\text{B3})$$

The largest value obtained with different bin sizes is kept as  $\beta_r$ .

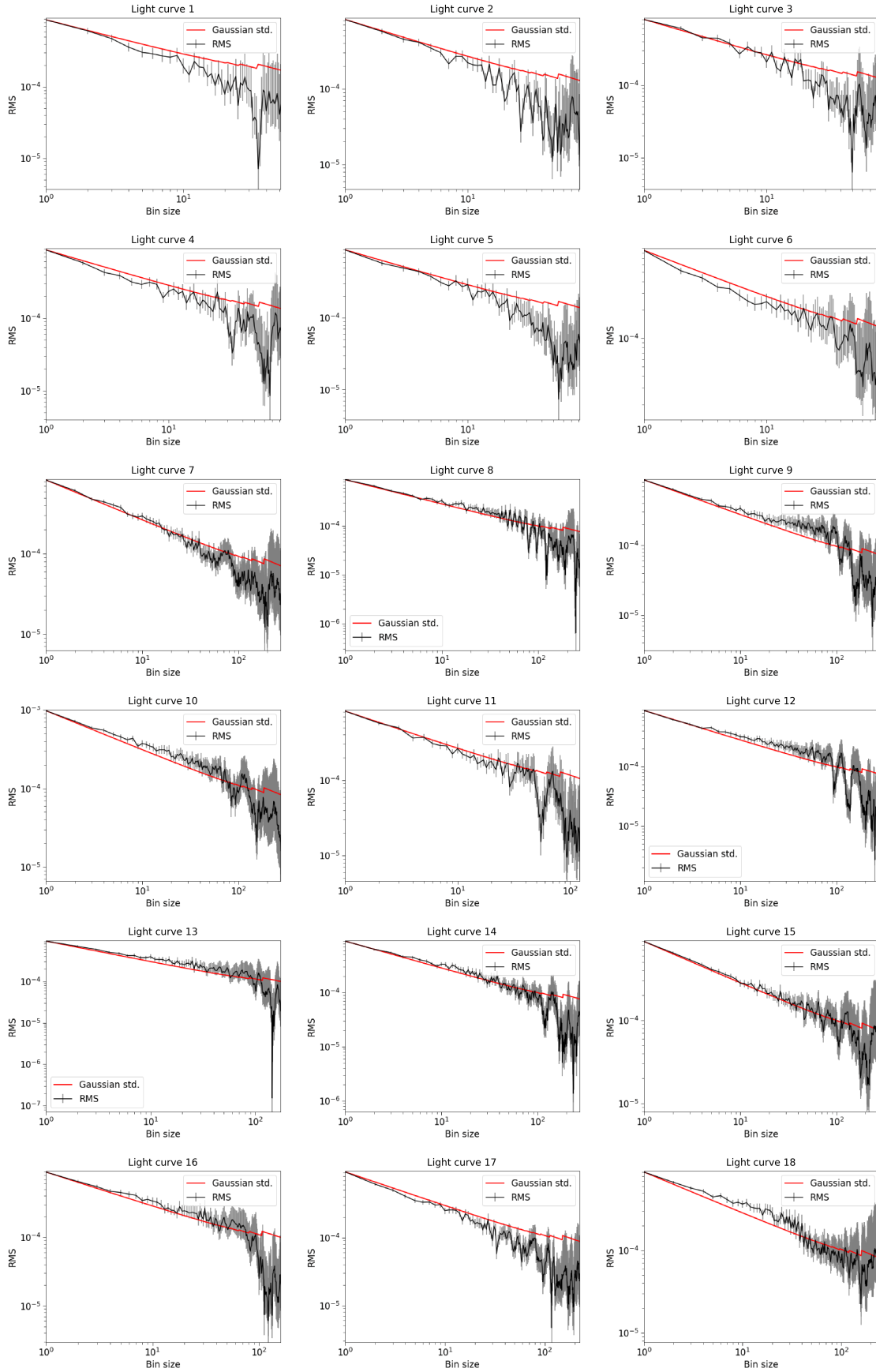


**Figure B1.** Binned residuals RMS (black curves with grey error bars) vs. bin size for the first eighteen *Spitzer*/IRAC light curves. The red curves are the expected RMS for Gaussian noise.



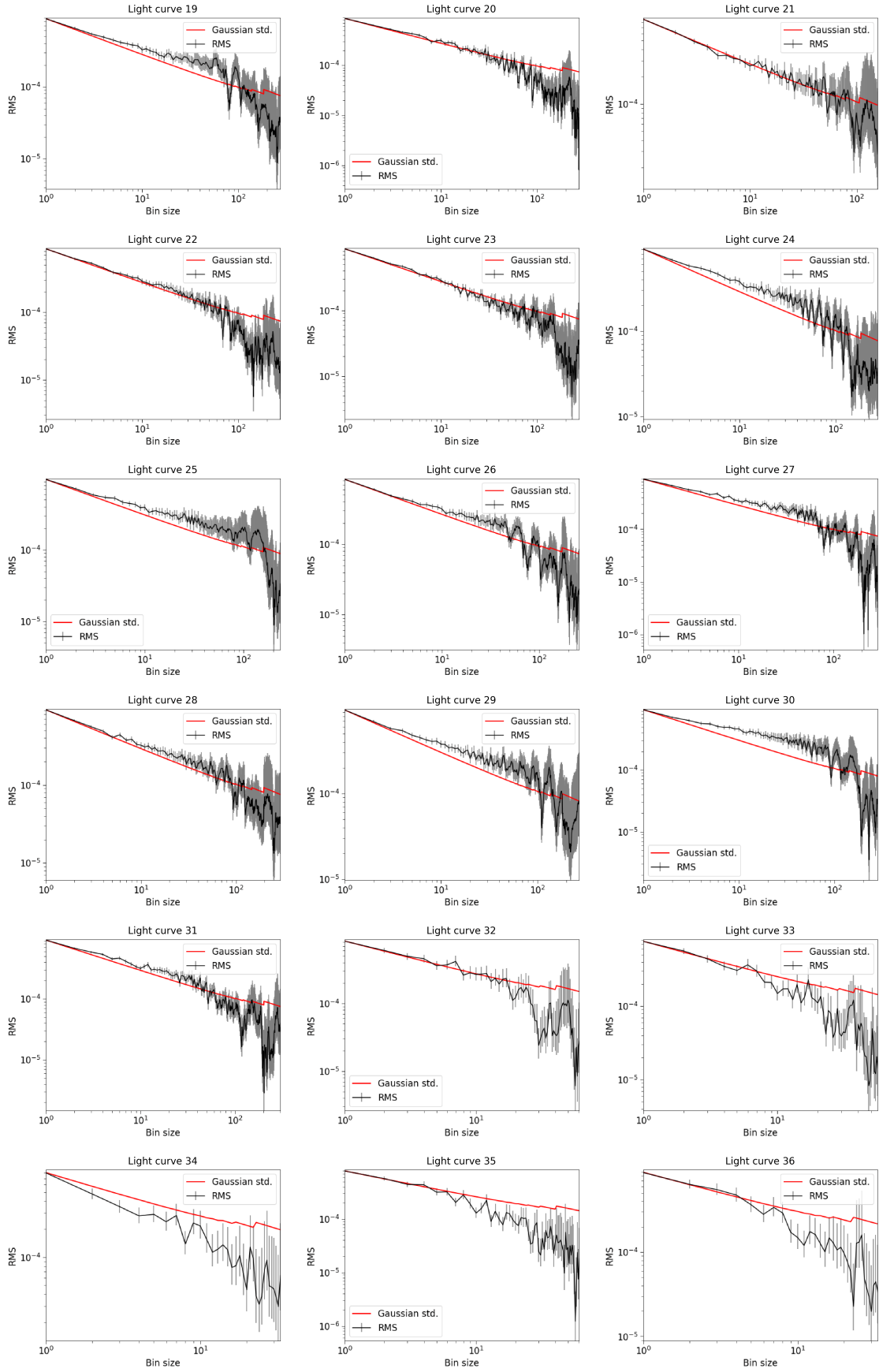
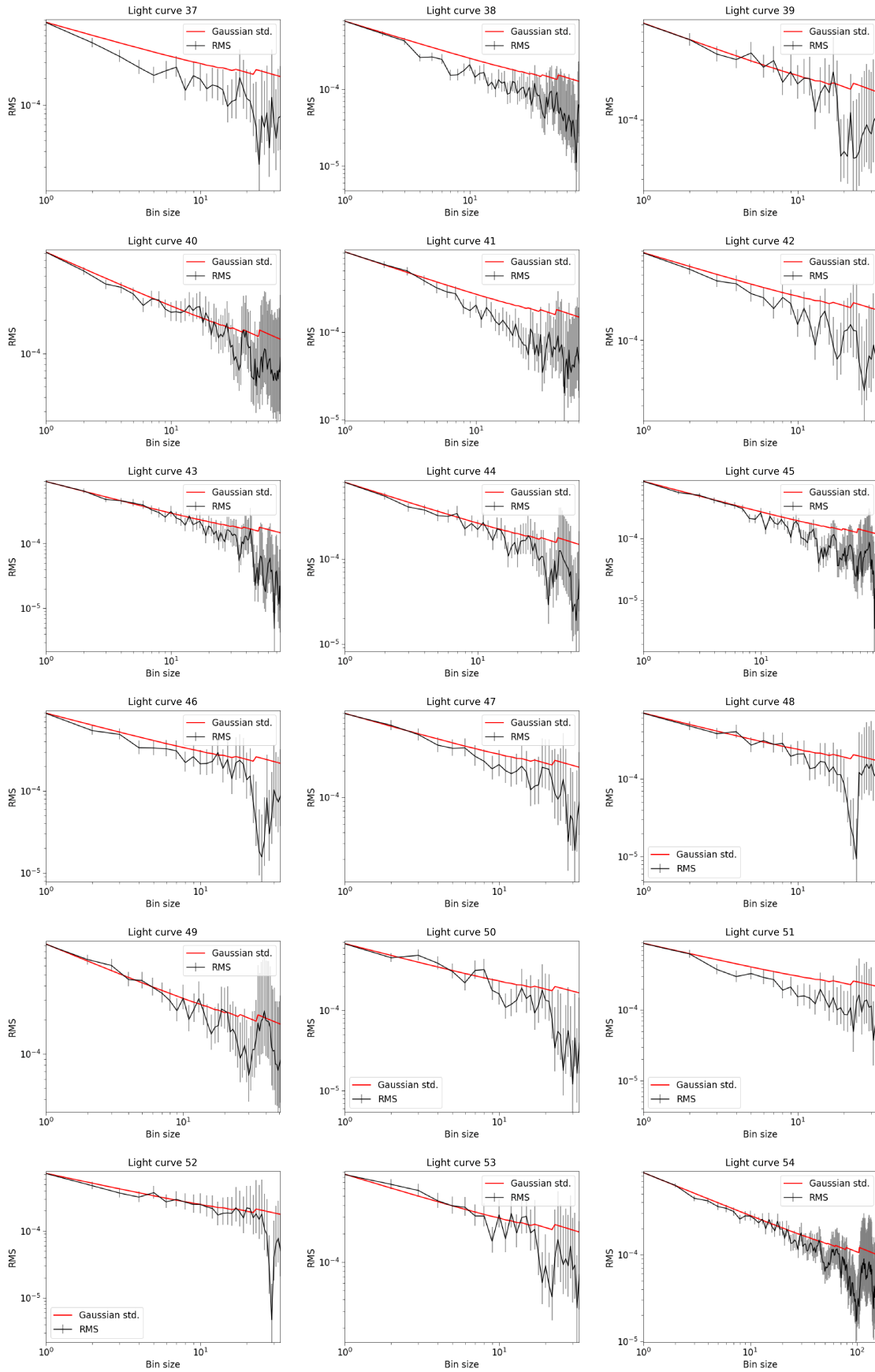


Figure B2. Same as Fig. B1, but for light curves 19 to 36.



**Figure B3.** Same as Fig. B1, but for light curves 37 to 54.

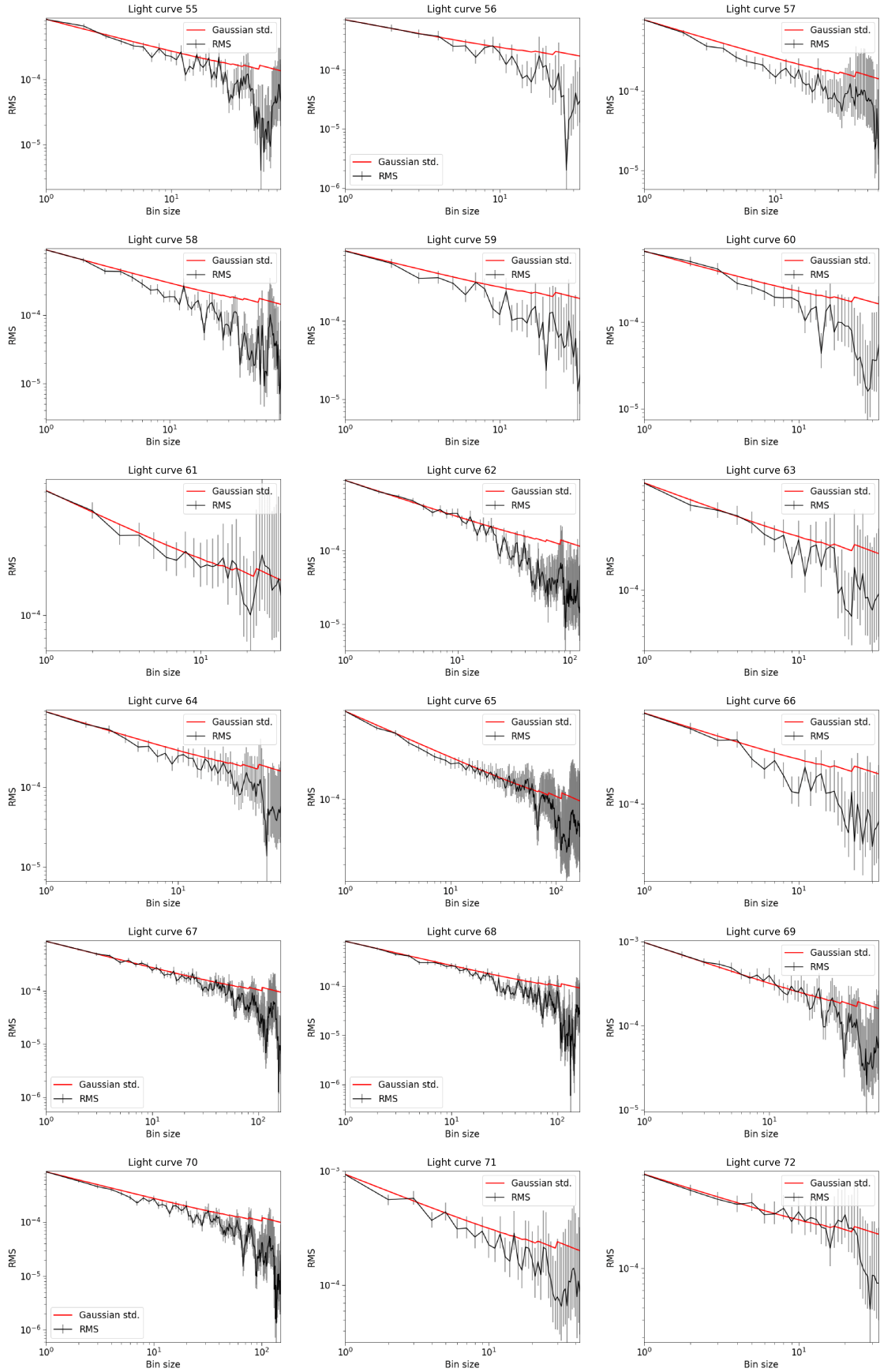
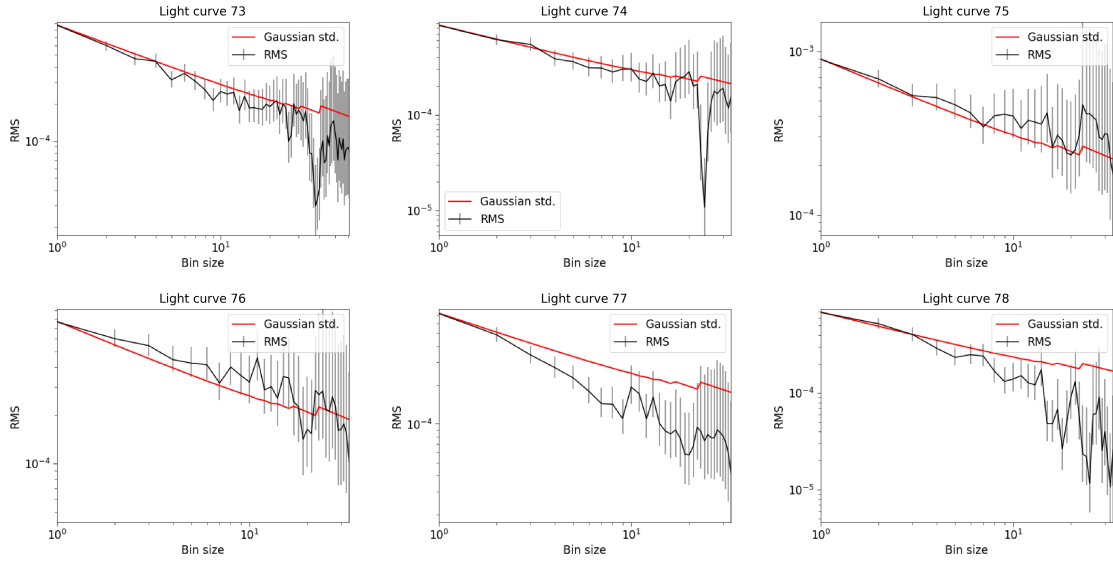


Figure B4. Same as Fig. B1, but for light curves 55 to 72.



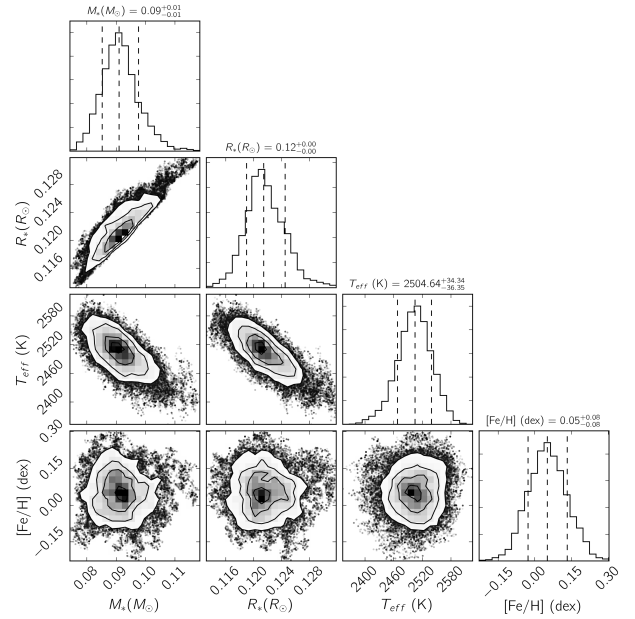
**Figure B5.** Same as Fig. B1, but for light curves 73 to 78.

## B2 Cross-correlation plots of the posterior PDFs

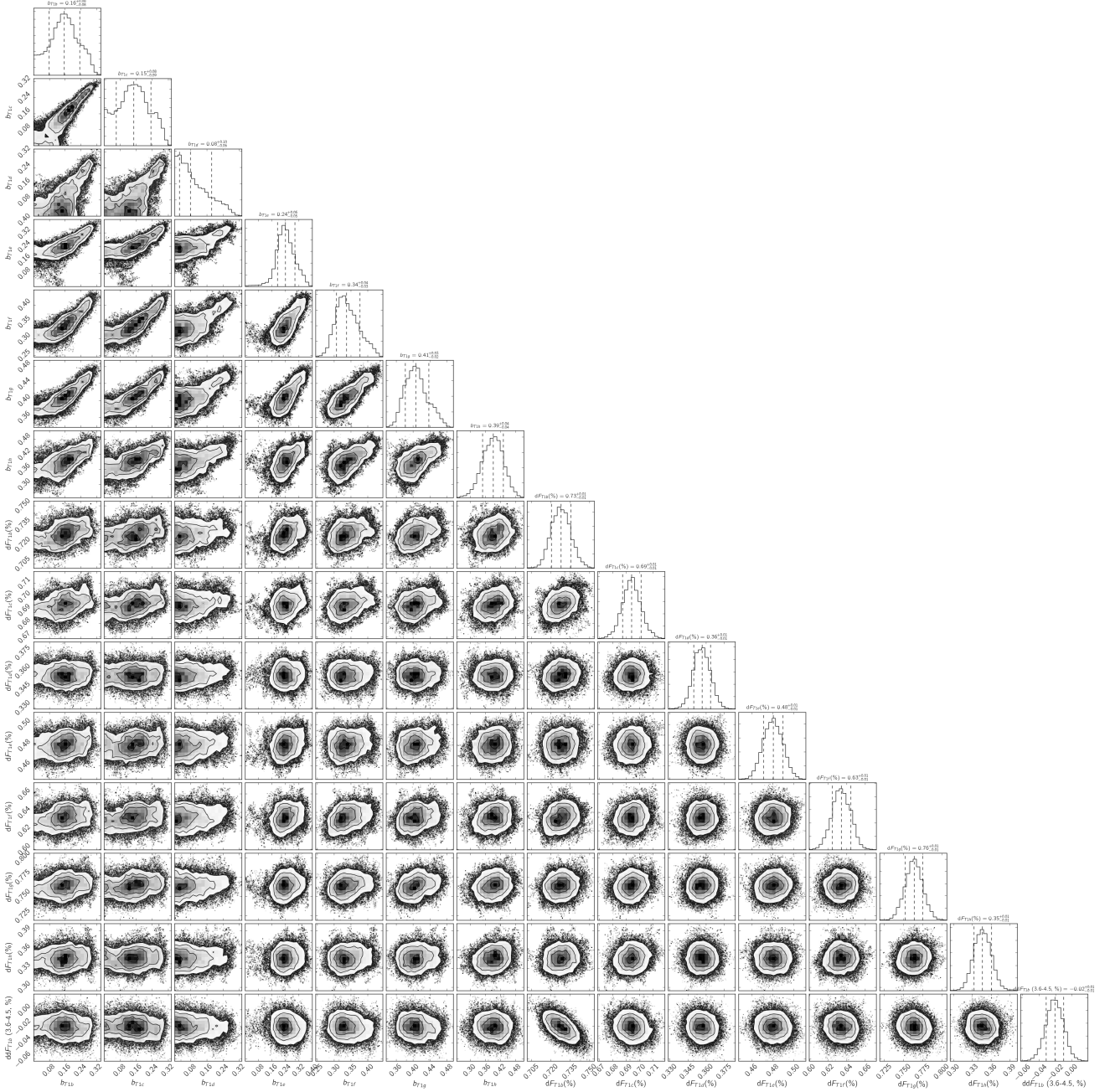
Fig. B6 shows the cross-correlation of the posterior parameters for the star from the global analysis made using `corner.py` (Foreman-Mackey 2016). Since the transit duration-period relation constrains the density of the star strongly, the mass and radius are strongly correlated. As the luminosity prior is strongly constrained, the uncertainty in radius is anti-correlated with the effective temperature. The metallicity correlates weakly with the other stellar parameters.

Fig. B7 shows the correlations between transit impact parameter and depth. As a common density for the star was used for all the transits, the impact parameters are strongly correlated as they anti-correlate with the transit durations, while the durations are well constrained by the data, and as zero eccentricity was assumed for the planet orbits. The depths correlate with the impact parameters as larger impact parameters have transit chords with lower surface brightness (due to limb-darkening), requiring a larger planet to cause the same transit depth.

The limb-darkening parameters and transit times correlate weakly with all of the other parameters, so we have not included these in the cross-correlation plots.



**Figure B6.** Cross-correlation plots and histograms of the posterior PDFs deduced for the stellar parameters from our global analysis.



**Figure B7.** Cross-correlation plots and histograms of the posterior PDFs of the transit depths and impact parameters for the seven planets, as well as the difference in transit depth of planet TRAPPIST-1b between IRAC channel 1 and channel 2.

**B3 Median values of the residuals in and out of transit**

Table B1: Median values ( $\text{median}_{\text{in}}$ ,  $\text{median}_{\text{out}}$ ) and median absolute deviations ( $\sigma_{\text{in}}$  and  $\sigma_{\text{out}}$ ) of the residuals in and out of transit, using the residuals from the global analysis. The last column gives the significance of the difference between  $\text{median}_{\text{in}}$  and  $\text{median}_{\text{out}}$ , computed as  $\frac{|\text{median}_{\text{in}} - \text{median}_{\text{out}}|}{\sqrt{\sigma_{\text{in}}^2 + \sigma_{\text{out}}^2}}$ .

Planet	Epoch	$\text{median}_{\text{in}}$ [ppm]	$\sigma_{\text{in}}$ [ppm]	$\text{median}_{\text{out}}$ [ppm]	$\sigma_{\text{out}}$ [ppm]	Significance of the difference [ $\sigma$ ]
b (3.6 $\mu\text{m}$ )	322	-188	421	213	600	0.55
	326	-371	415	33	488	0.63
	327	449	287	26	620	0.62
	330	-9	350	-107	522	0.16
	333	-107	522	151	588	0.33
	334	-27	587	143	350	0.25
	335	158	530	90	416	0.10
	338	445	637	162	761	0.29
	339	82	340	-153	334	0.49
	341	295	293	-45	421	0.66
	342	-407	635	219	579	0.73
b (4.5 $\mu\text{m}$ )	78	133	420	-290	464	0.68
	86	-32	344	362	390	0.76
	93	-240	303	-192	740	0.06
	218	-265	407	350	588	0.86
	219	279	527	-318	413	0.89
	220	-386	353	194	550	0.89
	222	-406	583	90	570	0.61
	224	104	519	-240	659	0.41
	225	-328	471	179	612	0.65
	226	-136	372	196	480	0.55
	227	-512	354	-361	621	0.21
	228	192	279	-188	423	0.75
	229	-226	831	-296	338	0.08
	230	-242	732	-684	624	0.46
	231	89	979	122	384	0.03
	318	-59	382	-430	606	0.52
	320	182	379	-67	473	0.41
	321	-229	466	-27	669	0.25
	324	226	417	14	561	0.30
	325	208	553	199	538	0.01
328	-145	700	110	530	0.29	
332	-45	530	-259	617	0.26	
336	334	669	-41	1003	0.31	
340	359	770	368	362	0.01	
c	70	126	475	11	618	0.15
	71	242	302	-171	404	0.82
	152	-331	251	-645	360	0.71
	153	102	405	-85	701	0.23
	154	512	538	75	964	0.40
	155	345	623	-11	658	0.39
	156	-92	684	53	596	0.16
	157	-167	742	-400	794	0.21
	158	-89	371	-311	750	0.27
	159	201	653	-168	391	0.48
	160	-112	380	-113	780	0.00
	215	124	602	-264	379	0.55
	216	340	664	-165	676	0.53
	217	-233	536	259	779	0.52
	218	13	547	-82	612	0.12
219	83	721	-79	452	0.19	
220	-32	472	96	670	0.16	

*Continued on next page*

Table B1 – continued from previous page

Planet	Epoch	median <sub>in</sub> [ppm]	$\sigma_{in}$ [ppm]	median <sub>out</sub> [ppm]	$\sigma_{out}$ [ppm]	Significance of the difference [ $\sigma$ ]
	221	-208	711	18	398	0.28
	222	333	501	-126	576	0.60
	223	-241	509	286	614	0.66
	224	90	772	-43	560	0.14
	225	-229	561	-79	376	0.22
	226	-71	602	-179	588	0.13
	227	-93	556	-297	734	0.22
	228	345	777	-98	333	0.52
	229	14	507	-128	466	0.21
	230	399	746	-115	559	0.55
d	-4	-159	754	260	733	0.40
	-3	110	472	112	551	0.00
	-2	-59	849	-103	674	0.04
	-1	61	593	-5	409	0.09
	0	-83	538	-96	669	0.02
	33	45	580	-63	721	0.12
	34	-73	511	180	579	0.33
	35	-87	723	23	451	0.13
	36	157	428	185	478	0.04
	37	313	652	-118	478	0.04
	38	-18	727	189	656	0.21
	39	-131	320	292	425	0.80
	40	312	720	206	573	0.12
	41	54	617	191	646	0.15
e	-1	-128	627	159	763	0.29
	0	-316	487	87	540	0.55
	24	218	500	-257	446	0.71
	25	-257	446	-49	693	0.25
	26	-149	637	234	559	0.45
	27	234	606	-392	508	0.79
	28	-201	695	334	580	0.59
	29	-251	531	-5	736	0.27
f	-2	-235	635	27	512	0.32
	-1	195	440	31	560	0.23
	0	40	632	159	726	0.12
	15	-205	516	-307	793	0.11
	16	-274	641	188	493	0.57
	17	-117	571	-203	612	0.10
	18	79	621	-196	541	0.33
g	-1	-235	635	-230	525	0.01
	0	555	531	377	557	0.23
	12	-48	336	+199	735	0.31
	13	-165	611	209	334	0.54
	14	143	609	-365	501	0.64
h	0	14	459	-26	646	0.05
	9	-27	540	-155	557	0.16

This paper has been typeset from a  $\text{T}_{\text{E}}\text{X}/\text{L}^{\text{A}}\text{T}_{\text{E}}\text{X}$  file prepared by the author.